Advances in Engineering Software 219 (2026) 104193

Contents lists available at ScienceDirect

Advances in Engineering Software

journal homepage: www.elsevier.com/locate/advengsoft

Research paper

A controllable domain-warped multifractal implicit-radius algorithm for generation of simulation-ready virtual aggregates

Dong Feng

Faculty of Civil Engineering, RWTH Aachen University, Mies-van-der-Rohe-Straße 1, Aachen 52074, Germany

ARTICLE INFO

Keywords:
Virtual aggregate generation
Particle shape modeling
Discrete element method (DEM)
Domain warping
Multifractal implicit-radius field

ABSTRACT

A controllable algorithm is developed to generate simulation-ready virtual aggregates using a domain-warped multifractal implicit-radius field. Fractional Brownian motion (FBM), ridged multifractals, Worley-type chipping, and layered anisotropy are integrated into a unified formulation, enabling decoupled and intuitive control of multiscale roughness, ridge sharpness, chipping intensity, and directional stratification within a single generator. The workflow automatically produces watertight triangular meshes and supports dimensional calibration based on principal component analysis (PCA) or an axis-aligned bounding box (AABB) to match prescribed particle proportions. Optional operations, including angular twisting, light smoothing, and bottom capping, are provided to enhance numerical stability and facilitate robust placement and contact handling in downstream simulations. A descriptor-driven calibration is further established to map generator inputs to roundness, boxiness, 3D solidity, and true sphericity, yielding interpretable parameter sensitivities and enabling targeted tuning toward the desired morphology. Morphological fidelity is validated against a 3D-scanned aggregate database using distribution-similarity measures and hypothesis testing, demonstrating close agreement at the population level. Discrete element method (DEM) simulations of Superpave gyratory compaction (SGC) are then conducted to assess engineering relevance, showing that the generated particles reproduce packing density evolution and gyration–height responses comparable to those of scan-based models. Overall, the proposed algorithm provides a practical bridge from controllable multifractal synthesis to validated, watertight, simulation-ready aggregate meshes for high-throughput numerical studies.

1. Introduction

Irregular aggregates govern interlocking, load transfer, and air void evolution processes in asphalt and concrete [1–3]. Natural lithology, weathering history, and crushing operations generate wide variability in particle morphology across sources [4–6]. Their 3D geometry, including overall size and proportions, angular ridges, and multiscale surface roughness, directly affects packing density, compaction trajectories, contact networks, and ultimately mixture stiffness and durability [7–9]. Because these effects accumulate from particle scale to mixture scale, even modest changes in angularity or roughness can shift force chain development [10–12], dilation behavior [13–15], and damage initiation under repeated loading [16,17]. In numerical modeling of pavement and concrete, representing this morphology with watertight, parameterizable meshes is a prerequisite for reproducible analyses [18–20]. Such representations also enable systematic parametric studies and uncertainty quantification, which are increasingly needed when mixtures are optimized for durability, cost, and sustainability constraints [21–23]. Establishing high-fidelity and statistically reliable aggregate databases is therefore essential for building numerical models that reproduce mechanical behavior with confidence [24,25]. In practice, the database must be sufficiently diverse to capture source-to-source variability while remaining compact enough for high-throughput simulation workflows.

Extensive efforts have been devoted to capturing or generating aggregate shape for simulation. High-resolution acquisition based on laser or structured-light scanning and close-range photogrammetry can reproduce sharp edges and chip-like defects and is widely used to build specimen-level digital twins for discrete element or finite element analyses [26,27]. However, particle-scale digitization alone does not guarantee simulation readiness, because contact detection [28,29], stability under gravity placement [30,31], and numerical convergence [32,33] all depend on mesh quality, watertightness, and consistent scale normalization. In parallel, two streams of virtual generation have emerged. Data-driven approaches use artificial intelligence to learn shape priors from scans or images and then sample new aggregates with

E-mail address: dong.feng@rwth-aachen.de.

https://doi.org/10.1016/j.advengsoft.2026.104193
Received 5 March 2026; Received in revised form 9 April 2026; Accepted 27 April 2026
Available online 7 May 2026

controllable global proportions [34,35]. Algorithmic approaches use explicit mathematics, including constructive solid geometry [36–38], superquadric perturbations [39–41], and random field perturbations based on fundamental geometries [42,43], to generate watertight meshes with tunable parameters.

Despite this progress, certain shortcomings still limit its routine application in numerical simulations. Scanning offers accuracy but scales poorly in cost and labor and often requires extensive mesh repair before analysis [44,45]. Moreover, the number of scanned particles is often insufficient to represent the tails of shape distributions that can strongly influence packing and segregation, especially when gradation spans multiple size fractions [46–48]. AI generators depend on training data and may blur high-frequency roughness or produce shapes with hidden artifacts [49,50], while mathematical recipes sometimes rely on a single noise primitive or ad hoc deformations that provide limited control over ridge prominence, chipping, and directional layering [51–53]. Mesh preprocessing can compromise watertightness or over-smooth sharp features, which degrades contact detection and forces excessive mesh density to retain detail [54–56]. This creates a practical trade-off between geometric fidelity and computational cost, and it can obscure which morphological traits are truly responsible for observed mechanical responses. A further limitation is the weak traceability from generator inputs to measurable geometric outcomes. In many studies the same target morphology can be achieved by multiple parameter combinations and the reporting of seeds, sampling protocols, and scale normalization is incomplete, which hampers reproducible comparisons and obscures how controllable inputs map to aggregate features of engineering interest [57–59].

To address the above limitations, the present study develops a compact, controllable, and simulation-ready algorithm for the automatic generation and evaluation of virtual aggregates. Each particle is represented as a radial graph over the unit sphere whose radius is driven by a domain-warped multifractal field that blends fractional Brownian motion (FBM), a ridged multifractal transform that enhances crest sharpness, and a Worley-type chipping term, with an additional layered anisotropy that introduces directional stratification. The key novelty of this study lies in the development of a unified domain-warped multifractal implicit-radius formulation that integrates multiscale roughness, ridge sharpening, chipping, and directional layering into a single controllable generator, while preserving explicit and largely decoupled parameter control over these distinct morphological characteristics. The construction yields watertight triangle meshes and decouples macro-dimensions from micro-roughness. Principal-axes (PCA) or axis-aligned dimension calibration, optional twist, bottom capping, and gentle smoothing prepare models for placement and analysis without eroding the fractal character. A further innovation is that the proposed workflow directly links procedural generation with simulation readiness by incorporating mesh-conditioning operations and dimensional calibration into the generation pipeline, rather than treating these steps as separate post-processing tasks. A calibration protocol maps control parameters to four standard shape descriptors, which enables targeted matching to scanned populations and sensitivity analysis across random seeds. Fidelity is evaluated in two ways. First, descriptor distributions from generated databases are compared to those from 3D-scanned aggregates through statistical testing. Second, Superpave gyratory compaction (SGC) simulations compare packing density and gyration–height responses across multiple cases. This combination of controllable multifractal synthesis, descriptor-based calibration, and engineering-scale discrete element method (DEM) validation distinguishes the present work from existing scan-based, AI-based, and conventional mathematical generation approaches. Results show close agreement between generated and scanned databases in both descriptor statistics and mixture-scale compaction behavior. The algorithm therefore provides a practical bridge from controllable multifractal generation to validated, analysis-ready meshes, enabling mechanistic mixture evaluation and performance-oriented modeling for civil and pavement materials.

The remainder of this paper is organized as follows. Section 2 details the proposed methodology, including the domain-warped multifractal implicit-radius field, the composite noise components, and the mesh-level processing steps that ensure watertight and simulation-ready geometries. Section 3 presents visualized examples to qualitatively demonstrate how each control parameter affects roughness, ridges, chipping, layering, and macro-scale deformation. Section 4 quantifies parameter effects using four shape descriptors and conducts sensitivity analyses, including the influence of mesh resolution and dimension calibration strategies. Section 5 establishes both 3D-scanned and algorithm-generated aggregate databases and evaluates their morphological agreement using distribution similarity metrics and statistical hypothesis testing. Section 6 assesses engineering relevance through discrete element simulations of SGC, comparing packing density and gyration–height responses between mixtures built from scanned and generated aggregates. Section 7 discusses the limitations of this study. Finally, Section 8 summarizes the main findings, discusses implications for simulation workflows, and outlines potential future work.

2. Methodology

In this section, the methodology of the proposed virtual aggregate generation algorithm is presented in a step-by-step manner. The objective is to formulate a reproducible pipeline that produces closed, watertight, and simulation-ready meshes while maintaining an explicit correspondence between control parameters and measurable geometric outcomes. The section first introduces the radial-graph surface representation and the domain-warped multifractal implicit-radius field, then describes the composite components responsible for multiscale roughness, ridge sharpness, chipping, and directional layering. Finally, mesh-level processing and calibration procedures are detailed, including optional macro-scale deformation, gentle smoothing, dimensional calibration, and bottom capping, to ensure numerical stability and consistent scaling for subsequent simulations.

The proposed algorithm procedurally constructs irregular aggregate geometries as follows. It generates irregular aggregate geometries by perturbing a base sphere with a domain-warped multifractal implicit-radius field driven by multifractal noise. The scalar field combines FBM, a ridged multifractal variant, and a cellular chipping term, further modulated by layered anisotropy. The resulting implicit surface is meshed and refined using global twist, shape-preserving smoothing, PCA fractal-shape dimension calibration, and bottom flattening with constrained Delaunay capping. This pipeline balances fractal realism (scale-rich relief, ridges, intermittency) with practical controllability (target length/width/height), producing closed, watertight meshes. Fig. 1 illustrates the overall workflow of the algorithm, and the detailed steps are described as follows.

2.1. Multifractal implicit-radius field and domain warping

This subsection first formalizes the fractal implicit-radius field that defines the aggregate surface. The aggregate is represented as a radially parameterized surface (a radial graph over the unit sphere), whose geometry is fully determined by a scalar radius function defined on directions, thereby providing a unified control of both global size and local roughness.

On the unit sphere S^2, let $\mathbf{u} = (u_x, u_y, u_z)^{\mathrm{T}}$ be a direction vector. A point on the aggregate surface $\mathbf{p}(\mathbf{u})$ is parameterized as:

$$\mathbf{p}(\mathbf{u}) = r_d(\mathbf{u})\mathbf{u}, r_d(\mathbf{u}) = r(1 + kN(\mathbf{u})), \tag{1}$$

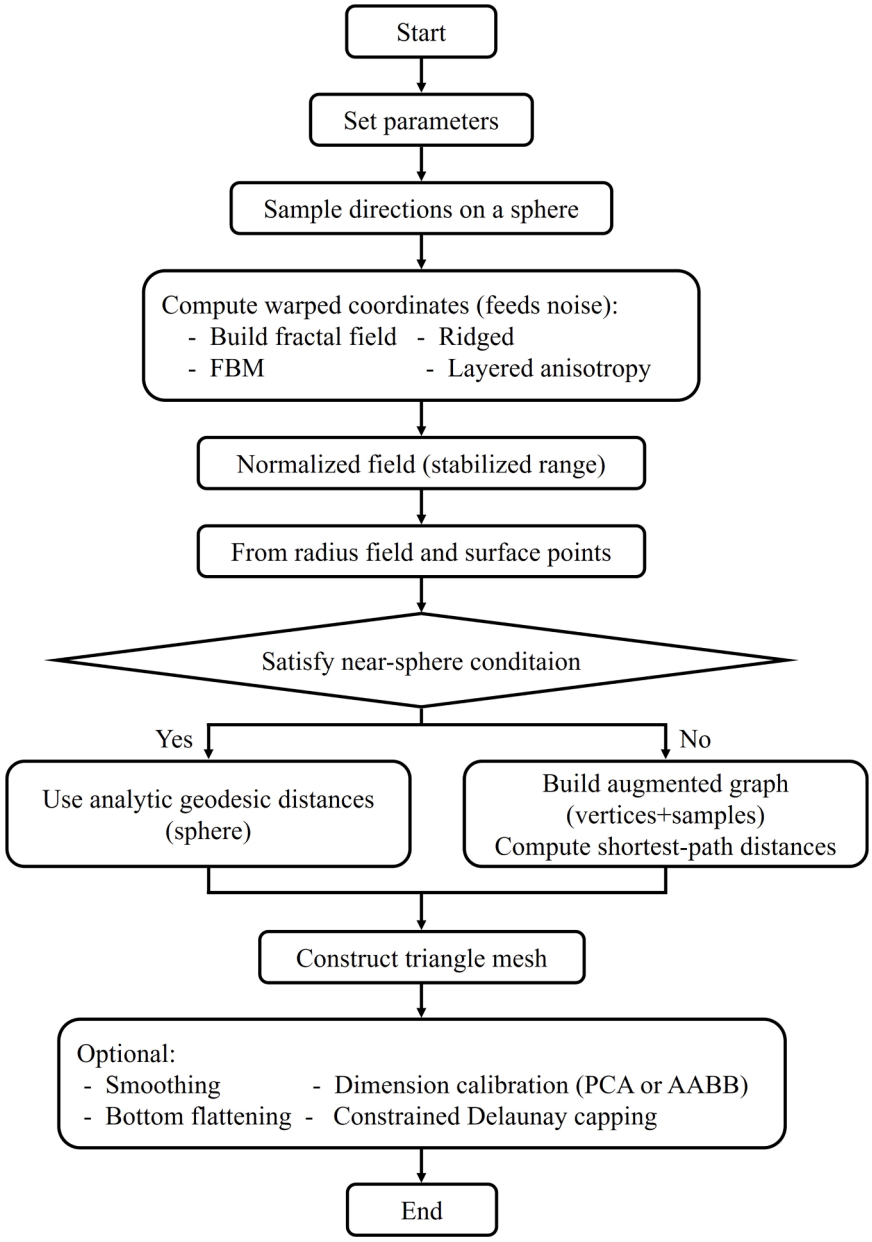

Fig. 1. Algorithm flowchart for generating virtual aggregates.

with base radius $r > 0$, perturbation coefficient $k \in [0, 1)$, and fractal scalar field $N(\mathbf{u}) \in [-1, 1]$. r_d denotes the radial distance (local radius) measured along the direction vector $\mathbf{u}$ from the origin. Modeling the radius as a fractal field over the sphere yields self-affine surface roughness typical of geological media.

To avoid axis-aligned artifacts and to introduce geologically plausible stretching, the method does not evaluate noise directly at $\mathbf{u}$. Instead, it warps the domain:

$$\mathbf{x}(\mathbf{u}) = s\mathbf{u} + \eta\mathbf{w}(s_w\mathbf{u}), \tag{2}$$

where s is the main scale, s_w is the warp scale, and η is the warp strength. The vector field $\mathbf{w} = (w_1, w_2, w_3)$ consists of three independently phased FBM channels, so the warped coordinate inherits fractal, self-affine variability across scales. Sampling the scalar field in this warped domain induces long-range correlations consistent with natural strata:

$$w_i(s_w\mathbf{u}) = \mathrm{FBM}(s_w\mathbf{u} + \boldsymbol{\delta}_i; O, \lambda, g), \text{with } i \in (1, 2, 3), \tag{3}$$

where $\boldsymbol{\delta}_i$ is the fixed translation (phase offset) of each FBM channel in the input space, O is the number of octaves, λ is lacunarity (frequency multiplier), and g is amplitude decay gain.

2.2. Composite noise field

Given the radially parameterized representation in Section 2.1, this subsection specifies the composite scalar noise field that drives the implicit-radius function. The method seeks a procedurally defined field that can reproduce a range of virtual aggregate morphologies by combining broadband roughness, sharp ridge-like features, and localized chipping within a single, tunable formulation.

With the warped fractal coordinates in place, the method defines a multifractal scalar field by mixing complementary components:

$$N(\mathbf{u}) = \alpha N_{FBM}(\mathbf{x}(\mathbf{u})) + \beta N_{ridge}(\mathbf{x}(\mathbf{u})) + \gamma N_{chips}(\mathbf{x}(\mathbf{u})), \tag{4}$$

where weights α, β, γ control the contribution of base fractal relief $N_{FBM}(\mathbf{x}(\mathbf{u}))$, ridge-enhanced multifractality $N_{ridge}(\mathbf{x}(\mathbf{u}))$, and intermittent chipping $N_{chips}(\mathbf{x}(\mathbf{u}))$.

Each term is introduced in turn to clarify its role. The FBM term $N_{FBM}(\mathbf{x}(\mathbf{u}))$ provides broadband undulations that yield self-affine fractal behavior:

$$N_{FBM}(\mathbf{x}) = \frac{1}{A_O}\sum_{o=0}^{O-1} g^o P(\lambda^o \mathbf{x}), A_O = \sum_{o=0}^{O-1} g^o, \tag{5}$$

where A_O is the amplitude weight of the O-th fractal octave, $P(\cdot)$ is 3D Perlin-like gradient noise, λ is lacunarity (frequency growth per octave), and g is gain (amplitude decay). This construction is a classical self-similar/multiplicative cascade approximation to FBM: its spectrum exhibits a power-law region, and the parameters (λ, g) jointly control the balance between low- and high-frequency content. Intuitively, larger lacunarity and gain increase high-frequency contributions, leading to a rougher surface appearance. For $\mathbf{x} = (x, y, z)^{\mathrm{T}}$, take the 8 hashed gradient tensors $\mathbf{g}_{ijk}$ of the containing lattice cell's corners, compute dot-products with corner-to-point tensors $\mathbf{d}_{ijk}$, and trilinearly interpolate using the quintic smoothstep [60]:

$$f(t) = 6t^5 - 15t^4 + 10t^3. \tag{6}$$

Then, sharp edges are accentuated via a ridged multifractal transform $N_{ridge}(\mathbf{x})$:

$$N_{ridge}(\mathbf{x}) = \frac{1}{A_O}\sum_{o=0}^{O-1} g^o (1 - |P(\lambda^o \mathbf{x})|)^2, \tag{7}$$

where the non-linear "ridge" mapping introduces multifractal intermittency (heavy-tailed gradients and localized singularities), enriching high-crested, facet-like features beyond Gaussian FBM and thereby increasing perceived multifractal complexity.

From Worley distances to the nearest (F_1) and second (F_2) feature points, the method defines the chipping term [61]:

$$N_{chips}(\mathbf{x}) = [1 - (F_2(\mathbf{x}) - F_1(\mathbf{x}))]_+^{\kappa} - \mu, \tag{8}$$

where $[\cdot]_+ = \max(\cdot, 0)$; κ is the sharpness exponent, which controls the nonlinear sharpening of Worley's decay signal based on $F_2 - F_1$; $\mu = \mathbb{E}[\cdot]$ removes bias (zero-mean). Intuitively, $F_2 - F_1$ is small near cell boundaries; transforming $1 - F_2 - F_1$ and applying a power emphasizes concave chipping along joint boundaries.

Bedding is then imprinted by modulating N multiplicatively:

$$N(\mathbf{u}) \leftarrow N(\mathbf{u}) \cdot [1 + A_L \sin(2\pi f_L \hat{\mathbf{n}} \cdot \mathbf{x}(\mathbf{u}))], \tag{9}$$

where $A_L \geq 0$ is layer modulation amplitude, $f_L \geq 0$ is layer spatial frequency, and $\hat{\mathbf{n}}$ is the unit direction of bedding (layer normal) with [1,1,1].

Finally, to avoid negative radius and outliers, the mixed field is linearly scaled into $[-1, 1]$:

$$N(\mathbf{u}) \leftarrow \frac{N(\mathbf{u})}{\max_{\mathbf{u}} |N(\mathbf{u})| + \varepsilon}, \tag{10}$$

where $\varepsilon > 0$ is a small numerical constant to avoid division by zero.

2.3. Mesh-Level geometry processing

After the implicit surface has been defined by the composite noise field, a set of mesh-level operations is applied to convert the raw geometry into a robust representation suitable for subsequent numerical use. This subsection focuses on post-generation processing that preserves the intended multiscale morphology while improving geometric validity, scaling consistency, and placement stability. Specifically, an optional global twist is introduced to impose coherent macro-scale deformation without altering the underlying texture statistics, followed by light smoothing to suppress isolated spikes and improve triangle quality. Dimensional calibration is then performed so that the mesh matches prescribed target proportions using either principal-axis alignment or an axis-aligned bounding-box strategy. Finally, bottom flattening and constrained triangulation are applied to create a stable support surface and to maintain a closed, watertight mesh required for reliable contact detection and simulation.

With the composite noise field fixed, the method next introduces an optional mesh-level twist that imparts coherent, macro-scale rotation. Let the twist axis be the unit vector **a**, $\mathbf{p}_0$ be a point on the axis, and ρ be the twist rate in rad/unit-length. For any vertex **p**, define:

$$s = \mathbf{a}^{\mathrm{T}}(\mathbf{p} - \mathbf{p}_0), \theta = \rho s, \tag{11}$$

where s is signed axial coordinate of point **p** along twist axis, and θ is the local twist angle applied to point **p**.

Using Rodrigues' formula [62], the rotation of **p** around **a** by θ is:

$$\begin{aligned} p^* &= p_0 + \underbrace{[(p - p_0)\cdot a]a)}_{axis-parallel} + \underbrace{(cos\theta v + sin\theta(a \times v), v}_{axis-orthogonal\ rotation} \\ &= (p - p_0) - [(p - p_0)\cdot a]a. \end{aligned} \tag{12}$$

Let $\mathbf{V} \in \mathbb{R}^{n\times 3}$ be vertex positions, and $\mathbf{W} = \mathbf{D}^{-1}\mathbf{A}$ be the one-ring mean adjacency (with undirected adjacency **A** and degree diagonal **D**). One iteration is:

$$\mathbf{V} \leftarrow \mathbf{V} + \lambda(\mathbf{W}\mathbf{V} - \mathbf{V}), \tag{13}$$

with $\lambda \in (0, 1)$ for each iteration.

For centered vertices $\mathbf{X} = \mathbf{V} - \overline{\mathbf{v}}$ ($\overline{\mathbf{v}} = \frac{1}{n}\sum_{i=1}^{n} \mathbf{v}_i = \left(\frac{1}{n}\sum x_i, \frac{1}{n}\sum y_i, \frac{1}{n}\sum z_i\right)$), the covariance is $\mathbf{\Sigma} = \frac{1}{n-1}\mathbf{X}^{\mathrm{T}}\mathbf{X}$. Performing an eigen decomposition yields:

$$\mathbf{\Sigma} = \mathbf{R}\mathrm{diag}(\sigma_1, \sigma_2, \sigma_3)\mathbf{R}^{\mathrm{T}},\ \sigma_1 \geq \sigma_2 \geq \sigma_3, \tag{14}$$

gives principal axes $\mathbf{R} = [\mathbf{e}_1, \mathbf{e}_2, \mathbf{e}_3]$. After PCA alignment, let the principal-space extents be:

$$\begin{aligned} \mathbf{p} &= (p_1, p_2, p_3) \\ &= (\max\mathbf{P}_{\cdot 1} - \min\mathbf{P}_{\cdot 1},\ \max\mathbf{P}_{\cdot 2} - \min\mathbf{P}_{\cdot 2},\ \max\mathbf{P}_{\cdot 3} - \min\mathbf{P}_{\cdot 3}),\ \mathbf{P} = \mathbf{X}\mathbf{R}. \end{aligned} \tag{15}$$

Then, exact fit calculates the scaling factor for each axis:

$$\mathbf{s} = \left(\frac{L}{p_1}, \frac{W}{p_2}, \frac{H}{p_3}\right), \tag{16}$$

and applies $\mathbf{V} \leftarrow (\mathbf{P}\mathrm{diag}(\mathbf{s}))\mathbf{R}^{\mathrm{T}} + \overline{\mathbf{v}}$, so that the final axis-aligned bounding box in the PCA frame matches the target dimensions exactly: *L, W, H*.

Using the same extents **p**, compute a single scale:

$$s = min\left\{\frac{L}{p_1}, \frac{W}{p_2}, \frac{H}{p_3}\right\}, \tag{17}$$

and applies $\mathbf{V} \leftarrow (s\mathbf{P})\mathbf{R}^{\mathrm{T}} + \overline{\mathbf{v}}$. The model is isotropically scaled so that its PCA-frame axis-aligned bounding box (AABB) fits entirely inside the target box, touching at least one face, without changing internal aspect ratios.

Let the target plane be $z = Z_0$. First translate so that min$z$ aligns with Z_0; then clamp any $z < Z_0$ to Z_0. To avoid a hard crease, define a transition band of thickness h_b; for $Z_0 < z < Z_0 + h_b$, apply linear blending:

$$\begin{cases} Z_0, & z < Z_0, \\ (1-t)z + tZ_0, & Z_0 \leq z < Z_0 + h_b,\ t = \dfrac{z - (Z_0 + h_b)}{Z_0 - (Z_0 + h_b)} \in [0, 1], \\ z, & \text{otherwise}. \end{cases} \tag{18}$$

From the current triangle mesh, take free boundary edges and select those lying on $z = Z_0$ to form one or more ordered closed loops $\{\mathscr{L}_i\}$. For each loop, project vertices to the (x, y) plane and perform constrained Delaunay triangulation $\mathscr{T}_i$ with loop edges as constraints. Add interior triangles as cap faces and merge with the original mesh:

$$F \leftarrow F \cup \bigcup_i \{\text{triangles inside } \mathscr{T}_i\}, \tag{19}$$

where F denotes the set of all triangular faces.

2.4. Implementation notes

These notes justify the specific stochastic primitives used earlier, connecting the theory of Section 2.2 to practical sampling on the mesh generated in Section 2.3. The Worley jitter hashing guarantees reproducibility for the chipping term, while the Perlin construction underpins both FBM and ridged multifractal components. Furthermore, pseudo-code for the algorithm is provided at the end of this section.

Decompose $\mathbf{x}$ as:

$$\mathbf{y} = \text{floor}(\mathbf{x}), \boldsymbol{\xi} = \mathbf{x} - \mathbf{y}, \tag{20}$$

where $\boldsymbol{\xi}$ denotes the fractional (local) coordinate of $\mathbf{x}$ within the cell.

Consider the $3 \times 3 \times 3$ neighborhood of integer cells around $\mathbf{y}$. Each cell $\mathbf{g} \in \mathbb{Z}^3$ contains a feature point $\mathbf{c} = \mathbf{g} + \boldsymbol{\delta}(\mathbf{g})$ with $\boldsymbol{\delta} \in [0, 1)^3$ generated via a 32-bit integer hash. Compute:

$$d^2(\mathbf{x}, \mathbf{c}) = \| \mathbf{x} - \mathbf{c} \|^2, \tag{21}$$

and update the nearest and second-nearest distances $F_1(\mathbf{x}) = \min d(\mathbf{x}, \mathbf{c})$, $F_2(\mathbf{x}) = \min_{d(\mathbf{x},\mathbf{c}) \neq F_1(\mathbf{x})} d(\mathbf{x}, \mathbf{c})$. The hash ensures reproducibility and uniform jitter.

Furthermore, based on the algorithmic principles involved in Sections 2.1, 2.2, and 2.3, the pseudo-code for the algorithm implementation is organized as follows: Algorithm 1.

3. Generate virtual aggregate visualization

This section presents virtual aggregate visualizations generated by the fractal–warped model described above. The objective is to enable qualitative observations of surface roughness, ridge features, and chipping characteristics under a unified perspective setting. Building upon the benchmark parameters, only one parameter is adjusted at a time to observe the impact of different parameters on the morphology of the virtual aggregate. Table 1 lists the control parameters for the numerical experiments, their benchmark values, corresponding symbols, and their meanings.

Table 1
Content overview for virtual aggregate studies.

Serial number	Symbol	Benchmark parameter value	Meaning
1	r	0.5	Base radius (reference dimension)
2	k	0.3	Perturbation coefficient (roughness amplitude)
3	s	1.5	Main scale
4	s_w	1.5	Warp scale
5	η	0.5	Warp strength
6	$\boldsymbol{\delta}_i$	[0,0,0]	Fixed translation (phase offset)
7	O	5	Number of octaves
8	λ	1.5	Lacunarity (frequency multiplier)
9	g	0.5	Amplitude decay gain
10	α	0.8	FBM weight
11	β	0.3	Ridge weight
12	γ	0.15	Chipping weight
13	κ	0.5	Sharpness exponent
14	A_L	0.15	Layer modulation amplitude
15	f_L	1	Layer spatial frequency
16	$\mathbf{a}$	[1,0,1]	Twist axis
17	$\mathbf{p}_0$	[1,0,0]	Base point on the axis
18	ρ	45°	Twist rate (rad per unit length)
19	$[L, W, H]$	[2,1.5,1]	Target length, width, height (from largest to smallest along the main axis)

Based on the same random seed, virtual aggregates are generated under different parameters, as shown in Fig. 2. All virtual aggregates employ a fixed viewing angle to enable independent assessment of multiscale roughness, ridge prominence, chipping, layering, and macro-deformation effects.

Increasing the base radius r warps the aggregate and reduces texture, but the relative positions of the textures remain unchanged. Increasing the perturbation coefficient k raises the amplitude of the fractal

Algorithm 1
Fractal-warped aggregate generation (with step relationships).

Input: base radius R, perturbation coefficient k; sampled directions $\{\mathbf{u}\}$, noise params (s, s_w,η, $\boldsymbol{\delta}_i$,O, λ, g, α, β, γ, κ, A_L,f_L); (optional) twist ($\mathbf{a}$, $\mathbf{p}_0$,ρ); target box (L, W, H).
Output: watertight triangle mesh (F, $\mathbf{V}$).
Warped coordinates (feeds all noise terms):
$\mathbf{x}(\mathbf{u}) = s\mathbf{u} + \eta\mathbf{w}(s_w\mathbf{u})$.
Fractal field $N(\mathbf{u})$ (drives radius):
$N(\mathbf{u}) = \alpha N_{FBM}(\mathbf{x}(\mathbf{u})) + \beta N_{ridge}(\mathbf{x}(\mathbf{u})) + \gamma N_{chips}(\mathbf{x}(\mathbf{u}))$.
Layered anisotropy (modulates $N(\mathbf{u})$):
$N(\mathbf{u}) \leftarrow N(\mathbf{u}) \cdot [1 + A_L \sin(2\pi f_L \hat{\mathbf{n}} \cdot \mathbf{x}(\mathbf{u}))]$.
Normalize (stabilizes radius):
$N(\mathbf{u}) \leftarrow \dfrac{N(\mathbf{u})}{\max_{\mathbf{u}} |N(\mathbf{u})| + \varepsilon}$.
Radius & surface (consumed by meshing):
$\mathbf{p}(\mathbf{u}) = r(\mathbf{u})\mathbf{u}$,
$r(\mathbf{u}) = R(1 + kN(\mathbf{u}))$.
Mesh construction:
from $\mathbf{p}(\mathbf{u})$ to (F, $\mathbf{V}$).
Optional global twist (macro deformation, after meshing):
$s = \mathbf{a}^{\mathrm{T}}(\mathbf{p} - \mathbf{p}_0)$,
$\theta = \rho s$.
Light smoothing (preserves fractal features; prepares for fitting):
$\mathbf{V} \leftarrow \mathbf{V} + \lambda(\mathbf{W}\mathbf{V} - \mathbf{V})$.
Dimension calibration (PCA or AABB):
align and scale to target $L \times W \times H$.
Bottom flattening (enables stable placement):
translate so $\min z = Z_0$; clamp $z < Z_0$ to Z_0; blend in a thin band.
Constrained Delaunay capping (produces watertight mesh):
triangulate interior of bottom boundary loops; append to F.
return (F, $\mathbf{V}$).

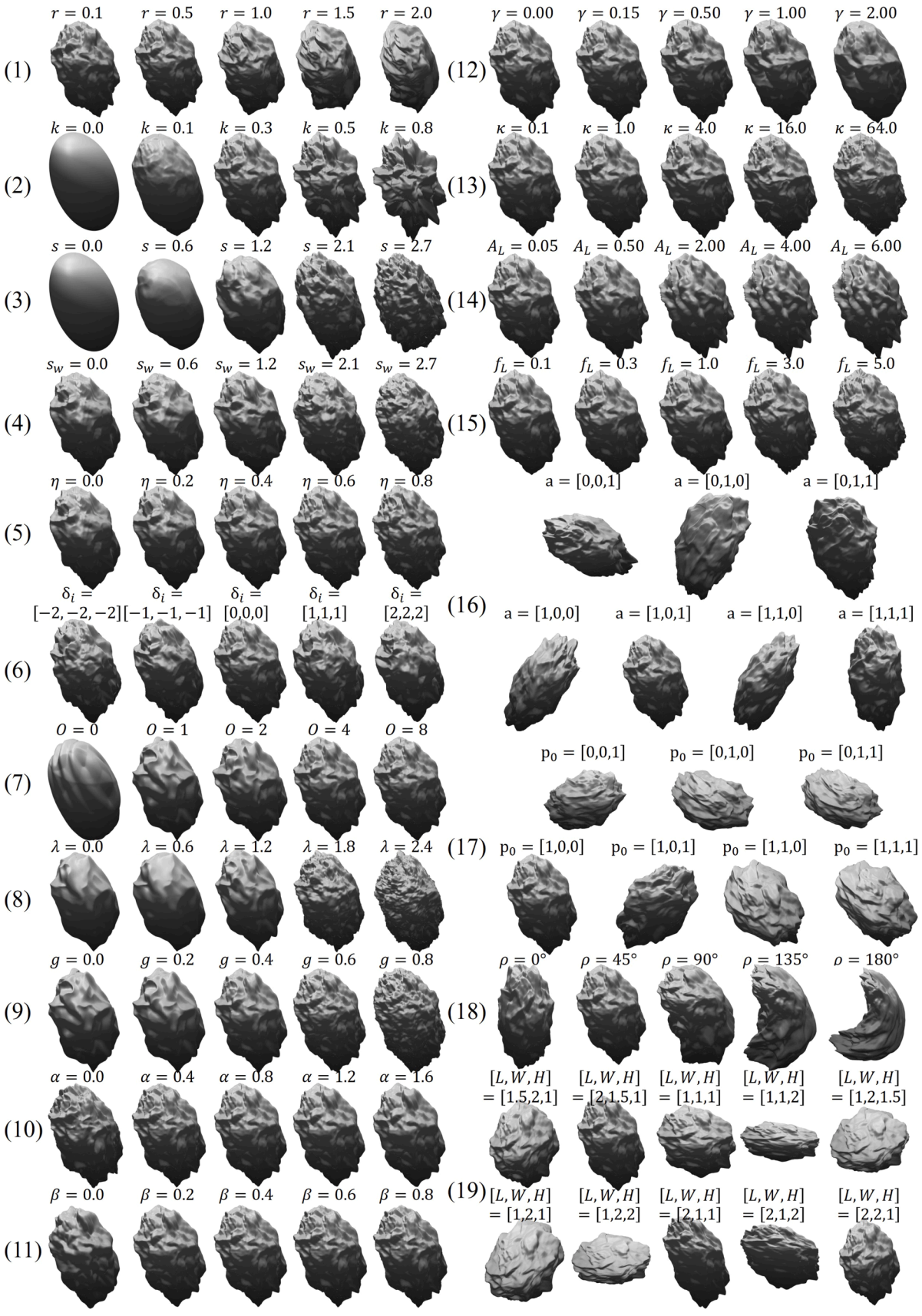

Fig. 2. Visualization for virtual aggregates under different parameters.

displacement and drives a continuous transition from a nearly smooth body to a visibly rough, blocky aggregate with stronger curvature contrasts. The main scale s controls the characteristic dimensions: a small s emphasizes broad-amplitude fluctuations, resulting in a smoother aggregate surface; whereas a large s modulates to finer wavelengths at the same amplitude, yielding a rougher aggregate surface. The warp scale s_w and warp strength η regulate domain distortion; low s_w and η preserve near-radial organization, while larger values advect structures, break spherical symmetry, and introduce gentle directional drift and asymmetry. Changing the phase offset δ_i produces different realisations with identical statistics, altering crest placement and silhouette while leaving the overall style intact.

Multiscale features are governed by the number of octaves O, lacunarity λ, and gain g. Adding octaves enriches the cascade of scales; increasing λ spreads spectral support and fills intermediate frequencies; higher g slows amplitude decay and strengthens micro-roughness. Relative contributions of the constituent fractal fields are tuned by the weights α (FBM) and β (ridged): larger α yields rounder, undulating relief with smoother transitions, whereas larger β sharpens crests and V-shaped valleys, shifting appearance toward craggy facets. The Worley chipping channel is controlled by γ and the sharpness exponent κ; increasing γ reduces the prevalence of pits and divots, while increasing κ converts soft depressions into crisp notches, increasing perceived angularity without changing their spatial distribution. Layered anisotropy parameters A_L and f_L imprint bedding-like bands that interact with ridges. Larger A_L enhances stratification contrast; larger f_L decreases layer spacing, producing tight laminations that modulate the fractal surface in a directionally consistent manner.

The optional global twist is defined by axis **a**, axis point $\mathbf{p}_0$, and twist rate ρ. Rotation operations reorient deformations relative to layered structures and ridge-like meshes; moving $\mathbf{p}_0$ off center skews the mass distribution; increasing ρ progressively curls the aggregate and exaggerates overhangs while leaving local roughness statistics unchanged. Finally, the dimension-calibration step aligns the mesh to its principal axes and scales it to the target box (L, W, H); modifying these targets alters aspect ratio and stance but does not affect the intrinsic fractal texture. Collectively, 2 demonstrates that the model provides orthogonal, interpretable controls over global size and pose, multiscale roughness, ridge prominence, chipping morphology, and stratified anisotropy.

4. Effect of control parameters on aggregate shape

This section focuses on investigating the effects of control parameters on aggregate shape. Four standard shape descriptors are first introduced to quantify morphology in a consistent and comparable manner, and their geometric meanings are illustrated for interpretation. A resolution study is then conducted to determine a practical triangular-mesh density that preserves descriptor fidelity while keeping computational cost manageable. Next, the influences of dimensional calibration strategy and angular twist are evaluated across typical shape classes to clarify their roles in macro-scale geometry control. Finally, a comprehensive sensitivity analysis is performed for the main control parameters using repeated random seeds, and the resulting trends are summarized to identify which parameters most strongly govern roundness, convexity, and sphericity, and which remain comparatively invariant.

First, to quantify how different control parameters influence the morphology of the generated virtual aggregates, four shape descriptors are defined and summarized in Table 2. These shape descriptors can be obtained through computational geometry techniques, with their visual representation shown in Fig. 3.

Additionally, based on the classification method proposed by Zingg, typical aggregate shape characteristics are grouped into four types [68]: cube, plate, column, and blade, as shown in Fig. 4a. Based on this classification, this study generates corresponding virtual aggregate types for further numerical research. The four types are separated by a

Table 2
Shape descriptors for aggregates, including their equations and notation.

Definition	Equation	Notation
Roundness [63–65]	$R = \frac{1}{r_{in}}\left(\frac{1}{N}\sum_{i=1}^{N} r_i\right)$	r_{in} denotes the radius of a sphere that fits entirely within the virtual aggregate and attains the largest possible size, r_i represents the radius of the corner-fitting spheres of the virtual aggregate, and N is the total number of such fitted spheres.
Boxiness [66]	$B = \frac{V_A}{V_{Box}} = \frac{V_A}{l_a l_b l_c}$	V_A represents the virtual aggregate volume, whereas V_{Box} represents the corresponding minimum bounding box volume enclosing the aggregate. l_a, l_b, and l_c denote the principal axis lengths in ascending order, from the shortest to the intermediate and the longest, respectively.
3D solidity [67]	$S_{3D} = \frac{V_A}{V_{conv}}$	V_{conv} denotes the smallest convex hull volume that completely contains the virtual aggregate.
True sphericity [63]	$TS = \frac{\pi}{S_A}\left(\frac{6V_A}{\pi}\right)^{\frac{2}{3}}$	S_A is the surface area of the virtual aggregate.

boundary defined as the 2/3 point between the flatness index (FI) and elongation index (EI):

$$FI = \frac{l_a}{l_b},$$

$$EI = \frac{l_b}{l_c}. \tag{22}$$

Mesh simplification plays an essential role in reducing the complexity of 3D virtual models while retaining their fundamental geometric features. However, the computation of shape descriptors is highly sensitive to the number of mesh elements (triangles). Therefore, this study first simplified virtual aggregates to a specified number of triangular meshes to investigate the sensitivity of shape descriptors. As shown in Fig. 4b, four different aggregate types are considered with triangular mesh counts of 51,200, 20,000, and 5000. Across the four aggregate types in Fig. 4b, boxiness B shows the smallest variation under mesh simplification, remaining essentially unchanged from 51,200 to 20,000 and still only marginally affected at 5000 triangles. By contrast, roundness R is the most resolution-sensitive descriptor: progressive decimation smooths high-curvature corners, enlarging the fitted corner spheres and producing a monotonic increase in R, especially for slender column- and blade-like shapes. 3D solidity S_{3D} and true sphericity TS exhibit modest upward drifts at very coarse resolution as concavities are reduced and surfaces become more convex. Taken together, these trends indicate that a working resolution of 20,000 triangles preserves descriptor fidelity while keeping computational cost moderate, with B essentially invariant and the remaining descriptors displaying predictable, monotonic behavior. Based on the above observations, an effective resolution of 20,000 triangles is selected as the benchmark for subsequent numerical analysis.

In this algorithm, both PCA and AABB methods can be used for dimensional calibration. Additionally, considering that angular twist significantly affects the shape of virtual aggregates, the influence of these two factors on aggregate shape is investigated. Four types of aggregates are generated based on the algorithm, as shown in Fig. 5. Although both methods aim to match the generated particle to prescribed target dimensions, they differ in their geometric basis. PCA-based calibration first aligns the aggregate with its principal inertia directions and then scales the particle in the corresponding principal frame, which is more closely related to the intrinsic mass distribution and dominant shape orientation of the aggregate. In contrast, AABB-based calibration is performed directly with respect to the axis-aligned bounding box, making it computationally simpler and more

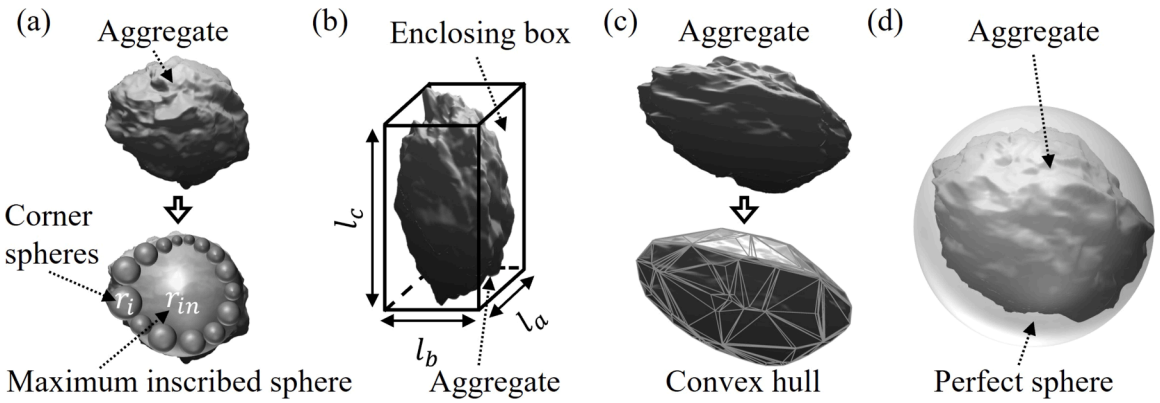

Fig. 3. Visual representation of virtual aggregate shape descriptors: (a) roundness, (b) boxiness describes the similarity between a virtual aggregate and its bounding box, (c) 3D solidity, (d) true sphericity.

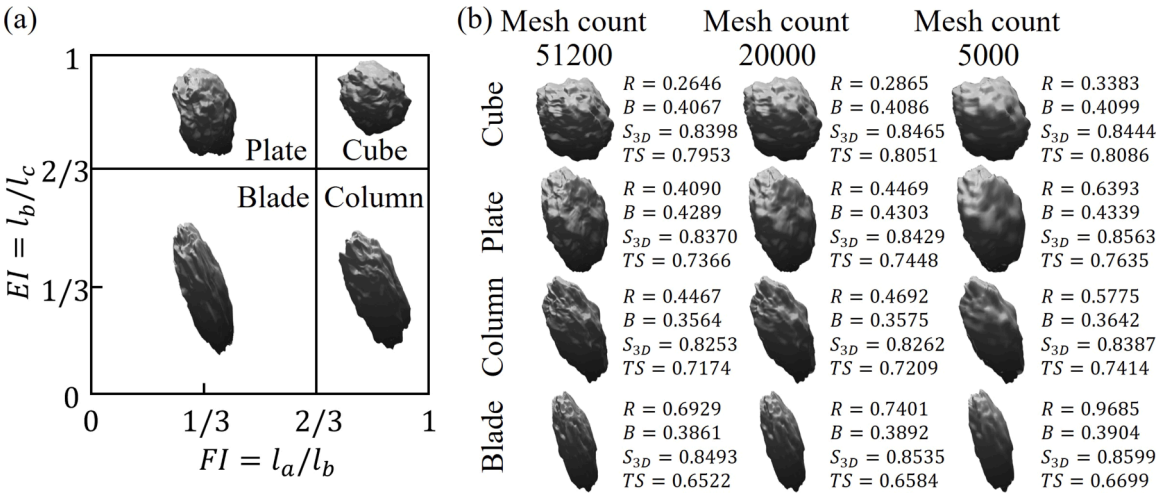

Fig. 4. Generation of different types of virtual aggregates: (a) aggregate classification, (b) effect of mesh simplification on aggregate shape.

straightforward, but also somewhat more sensitive to the current pose and local extremal vertices of the mesh.

For the four aggregate types, using PCA or AABB for dimension calibration produces very similar outcomes. Differences in B and S_{3D} are negligible and are not discussed further. For the cube type, AABB tends to yield slightly lower R and slightly higher TS than PCA across the tested ρ. For the plate type, AABB produces a small increase in R together with a small decrease in TS. For the column type, both R and TS are generally slightly lower under AABB than under PCA. For the blade, AABB gives slightly lower R and slightly lower TS. Overall, these differences remain limited, indicating that both calibration methods are capable of preserving the global morphological characteristics of the generated aggregates. The slightly larger deviations observed for elongated or slender shapes can be attributed to the fact that AABB is more directly affected by local geometric protrusions and pose-dependent envelope dimensions, whereas PCA provides a more shape-oriented scaling reference. From a practical perspective, PCA is advantageous when a morphology-consistent principal-axis representation is desired, while AABB remains useful when a simple bounding-box-based dimensional fit is preferred.

Varying the twist rate from 0° to 60° mainly changes the descriptors through controlled shear of the mass distribution while leaving the local fractal texture intact. Across types, R increases monotonically with ρ, whereas TS decreases gradually as the surface departs from the sphere-like reference. B exhibits no discernible monotonicity during the rotation process, with its values fluctuating slightly up and down. This aligns with its characteristic reliance on axis-aligned bounding volumes rather than fine-scale structural features. S_{3D} shows a mild downward trend at larger ρ due to the progressive loss of tight convexity. Sensitivity to twist is shape-dependent: column and blade types show the largest increase in R and the most pronounced reductions in TS, while cube and plate remain comparatively robust. These patterns confirm that calibration choice affects global dimensions weakly, whereas the twist parameter provides a convenient macro-control for modulating apparent elongation without compromising the underlying fractal character of the aggregates. Taken together, the comparison suggests that the two calibration methods are broadly consistent in descriptor-level outcomes, while PCA offers a slightly more stable and morphology-oriented scaling basis and AABB offers a simpler and more direct geometric implementation.

Then, a comprehensive investigation is conducted into the sensitivity of shape descriptors to control parameters. Numerical experiments are performed for the first 15 control parameters, with benchmark parameter values based on Table 1. 30 random seeds are generated at each sampling point, and the numerical results are averaged to obtain the computation result for the current sampling point. Subsequently, all sampling points are plotted as shown in Fig. 6.

The curves in Fig. 6 reveal distinct sensitivities of the four descriptors to the generative controls. R is the most sensitive indicator, while boxiness B consistently shows the least impact. S_{3D} and TS fall between these two. Varying r has only a minor impact: R shows a slight decline with increasing r, whereas B, S_{3D}, and TS remain nearly constant. k

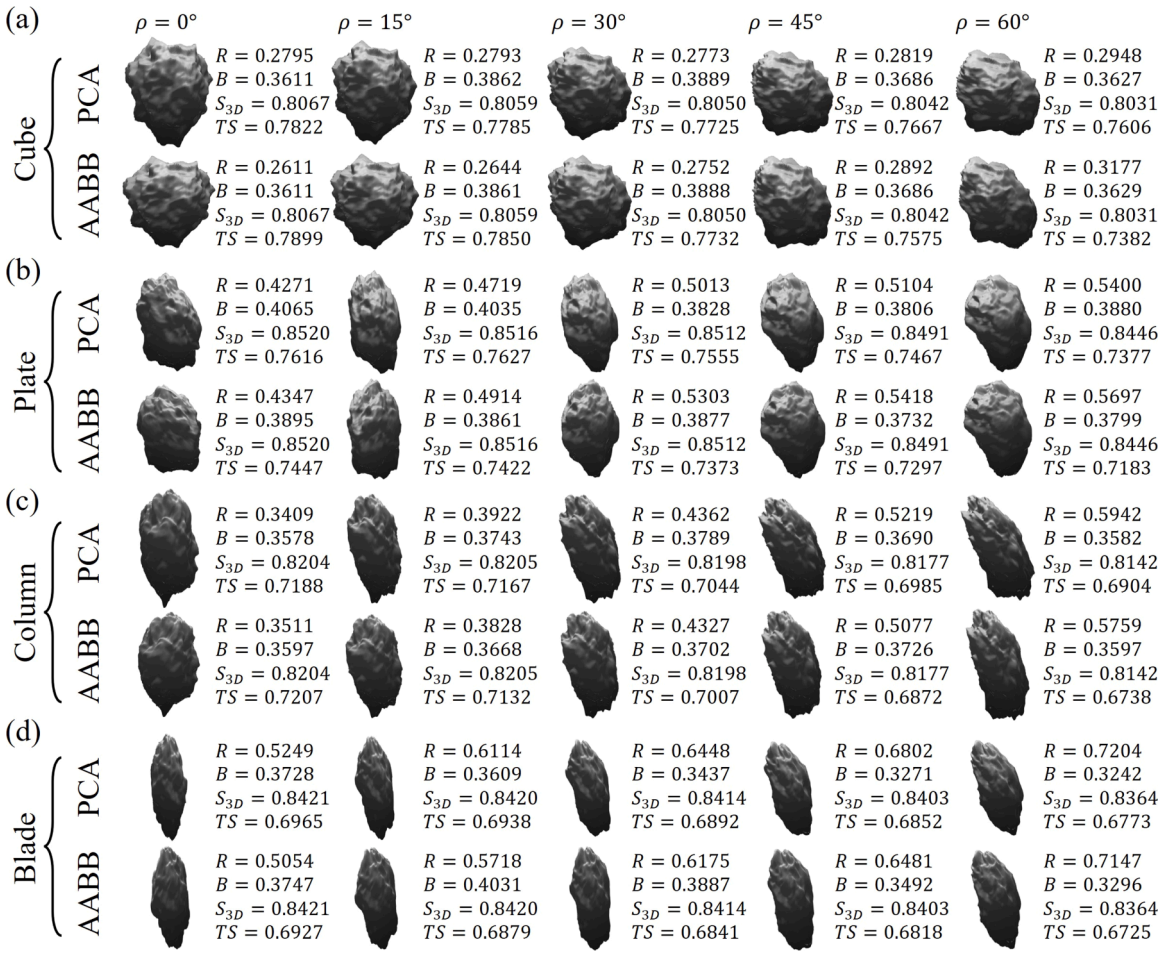

Fig. 5. Effects of dimension calibration and angular twist ρ on virtual aggregates: (a) visualization of cube aggregate for different angular twist angles, (b) visualization of plate aggregate for different angular twist angles, (c) visualization of column aggregate for different angular twist angles, (d) visualization of blade aggregate for different angular twist angles.

produces the strongest effect: R drops rapidly at small k as fine roughness emerges, then rebounds at high k when protrusions become more uniform; S_{3D} and TS decrease steadily as concavities deepen, and B changes only marginally. s also reduces R, S_{3D}, and TS as larger-wavelength relief grows, with only a small drift in B. Increasing s_w or η causes the R value to decrease rapidly, S_{3D} and TS values to decrease slightly, while B value shows negligible change. δ_i primarily rephases the noise and therefore causes only small local fluctuations in all metrics.

Multi-resolution controls modulate curvature in predictable ways. When O is below 5, the descriptor values exhibit a decreasing trend, stemming from finer detail representation. Meanwhile, λ demonstrates a pronounced threshold effect: when λ exceeds approximately 1, R value drops sharply, and both S_{3D} and TS show a downward trend as multi-scale voids emerge. For g, the effect on descriptor values is negligible before 0.4. After 0.4, as g increases, the values of R, S_{3D}, and TS decrease monotonically.

Mixing weights can adjust fractal field characteristics. Increasing α enhances R, S_{3D}, and TS values while slightly increasing B value, consistent with surfaces dominated by smoother folds. Raising β does the opposite, lowering R and nudging S_{3D} and TS downward as sharper crests and troughs form. As the edges become rounded, γ gradually increases the values of each descriptor; while κ progressively decreases the values of each descriptor by sharpening the edge corners. Layered anisotropy introduces controllable directional modulation. As layered wrinkles deepen, higher A_L values cause slight decreases in various values, while increased f_L primarily reduces the R value with negligible effects on B, S_{3D}, and TS.

Taken together, these results indicate that R provides the most sensitive gauge of roughness architecture, TS and S_{3D} capture the progressive loss of convexity with stronger or more multiscale perturbations, and B remains essentially invariant across the parameter space. This sensitivity separation is of practical value for directional calibration: k and s control the overall roughness intensity; O, λ, and g describe multiscale features; α, β, and γ adjust texture style, while A_L and f_L optimize anisotropic appearance while maintaining a limited impact on the overall volume proportion.

In addition, a supplementary space-filling screening procedure based on Latin hypercube sampling is presented in Appendix B to extend the descriptor-parameter exploration beyond the one-at-a-time (OAT) paths used in the main text, while noting that the present OAT analysis is primarily intended to reveal first-order trends rather than full interaction effects.

To further verify the practical utility of the descriptor-driven calibration, a closed-loop inverse-mapping validation is presented in Fig. 7, while the detailed computational procedure is provided in Appendix B. Three target descriptor vectors are selected from different regions of the descriptor space, namely {0.60, 0.45, 0.85, 0.75}, {0.70, 0.47, 0.90, 0.80}, and {0.75, 0.50, 0.90, 0.85}. For each target, the corresponding parameters are identified through the supplementary inverse-search procedure and then used to generate three aggregates under different random seeds. The resulting descriptor vectors are subsequently re-evaluated and compared with the prescribed targets.

As shown in Fig. 7, the generated aggregates remain close to the target descriptor levels in all three validation cases, demonstrating that

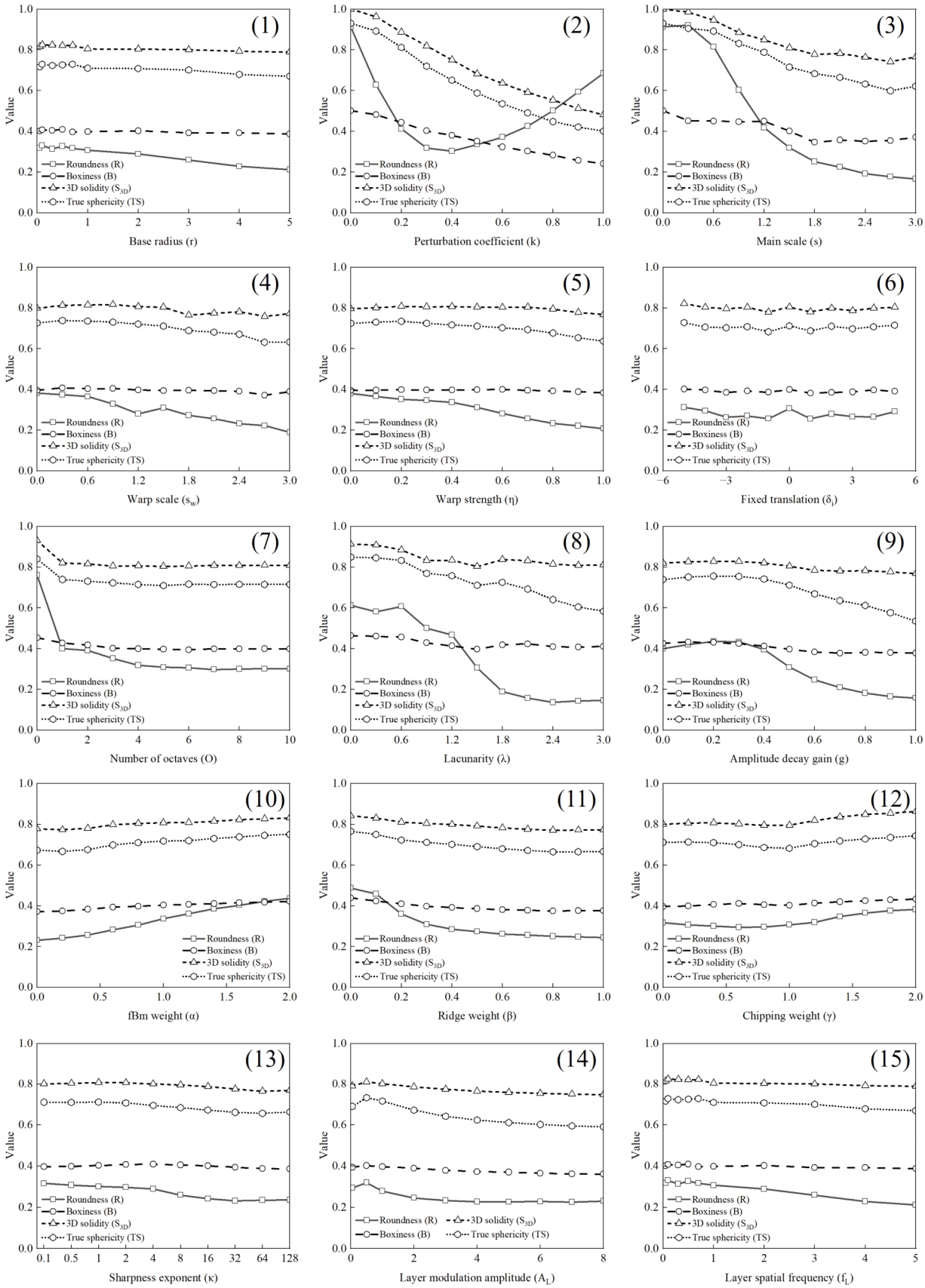

Fig. 6. Effects of different control parameters on aggregate shape descriptors (roundness, boxiness, 3D solidity, and true sphericity).

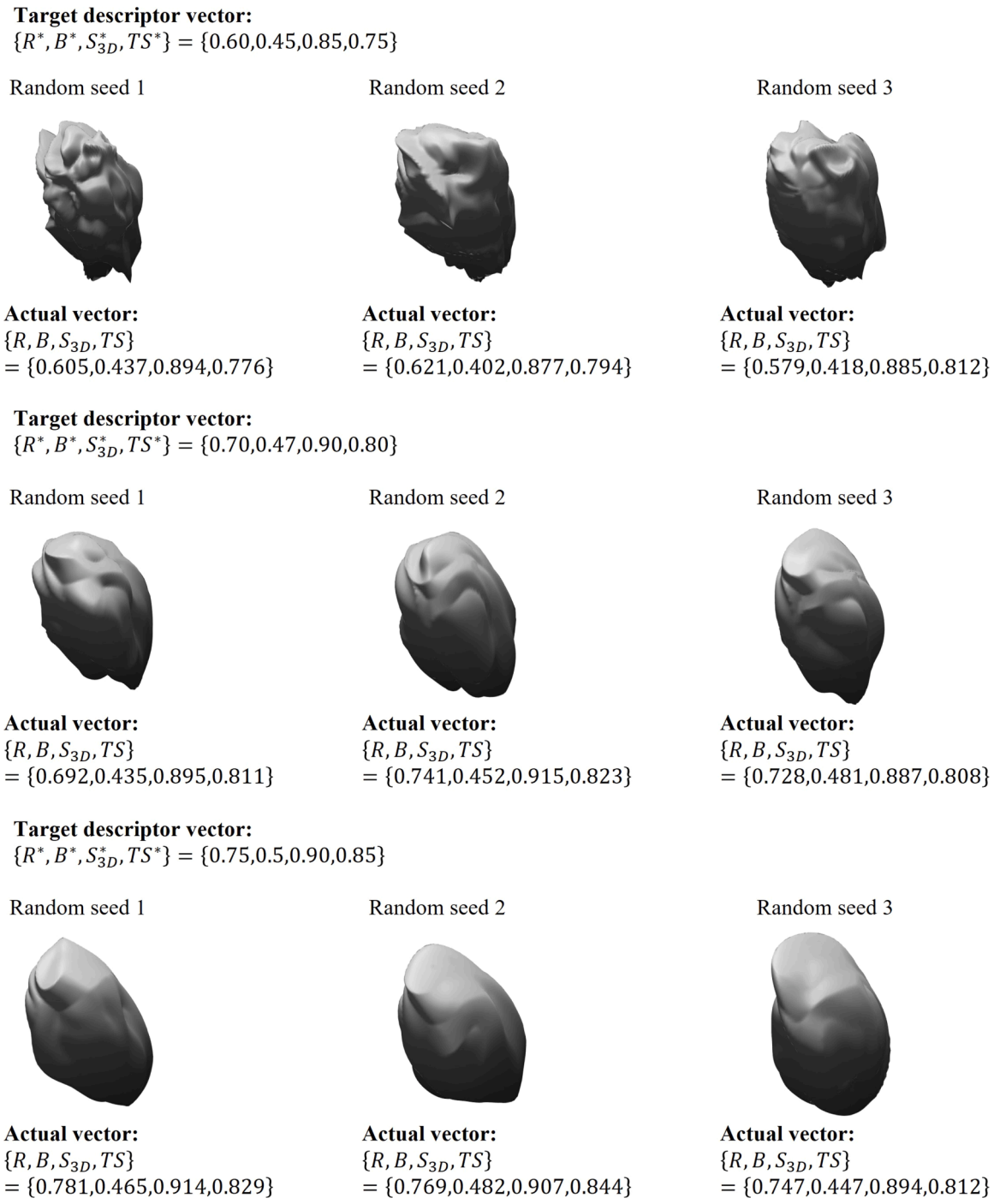

Fig. 7. Validation of inverse descriptor-to-parameter mapping through target-guided aggregate generation.

the proposed framework can be used not only for forward descriptor prediction, but also for inverse parameter identification and target-guided synthesis. For the first target vector, the achieved R values range from 0.579 to 0.621 around the target value of 0.60, while B remains slightly lower than the target 0.45 and both S_{3D} and TS are moderately higher than the prescribed values. For the second target vector, the agreement is generally closer, with R varying from 0.692 to 0.741, B from 0.435 to 0.481, S_{3D} from 0.887 to 0.915, and TS from 0.808 to 0.823, indicating that all four descriptors are reproduced within a relatively narrow band around the target. For the third target vector, the generated aggregates again preserve the intended descriptor level, although B and TS tend to be slightly underestimated in some seeds, whereas R and S_{3D} remain close to the targets.

An additional observation is that the seed-to-seed variability does not obscure the intended descriptor trend across the three cases. As the target vector moves toward higher R, B, and TS values, the generated particles exhibit correspondingly smoother and more rounded overall morphology, which is visually consistent with the descriptor progression. At the same time, the remaining deviations confirm that the inverse mapping is not strictly one-to-one, and small stochastic fluctuations still persist after parameter identification. Nevertheless, the results provide a direct end-to-end demonstration that the descriptor-driven calibration is practically effective for inverse design, because it can recover parameter sets that generate aggregates with descriptor values consistently close to the prescribed targets.

5. Establishment of virtual aggregate database

This section focuses on constructing the databases required for an objective, population-level validation of the proposed algorithm. A reference database is first established from three-dimensional scans so that real aggregate morphology is represented by consistent, measured samples with known provenance. A virtual database is then created using the proposed algorithm with a comparable sample size and size-fraction composition to enable direct population-level comparisons. The section subsequently describes the database organization and the evaluation protocol, in which morphological consistency is assessed using the selected shape descriptors together with distribution-based similarity measures and statistical hypothesis testing.

To ensure the robustness of the proposed algorithm, the morphology of the generated virtual aggregates should be comparable to that of real aggregates. To this end, this section first establishes an aggregate database based on 3D scanning. The morphological distributions in this reference database are then compared with those from an aggregate database produced by the proposed algorithm, in order to assess the algorithm's consistency and effectiveness. In this study, a 3D scanner is employed to capture real aggregates and generate corresponding virtual 3D models. The scanned raw aggregates are quarried from a site near

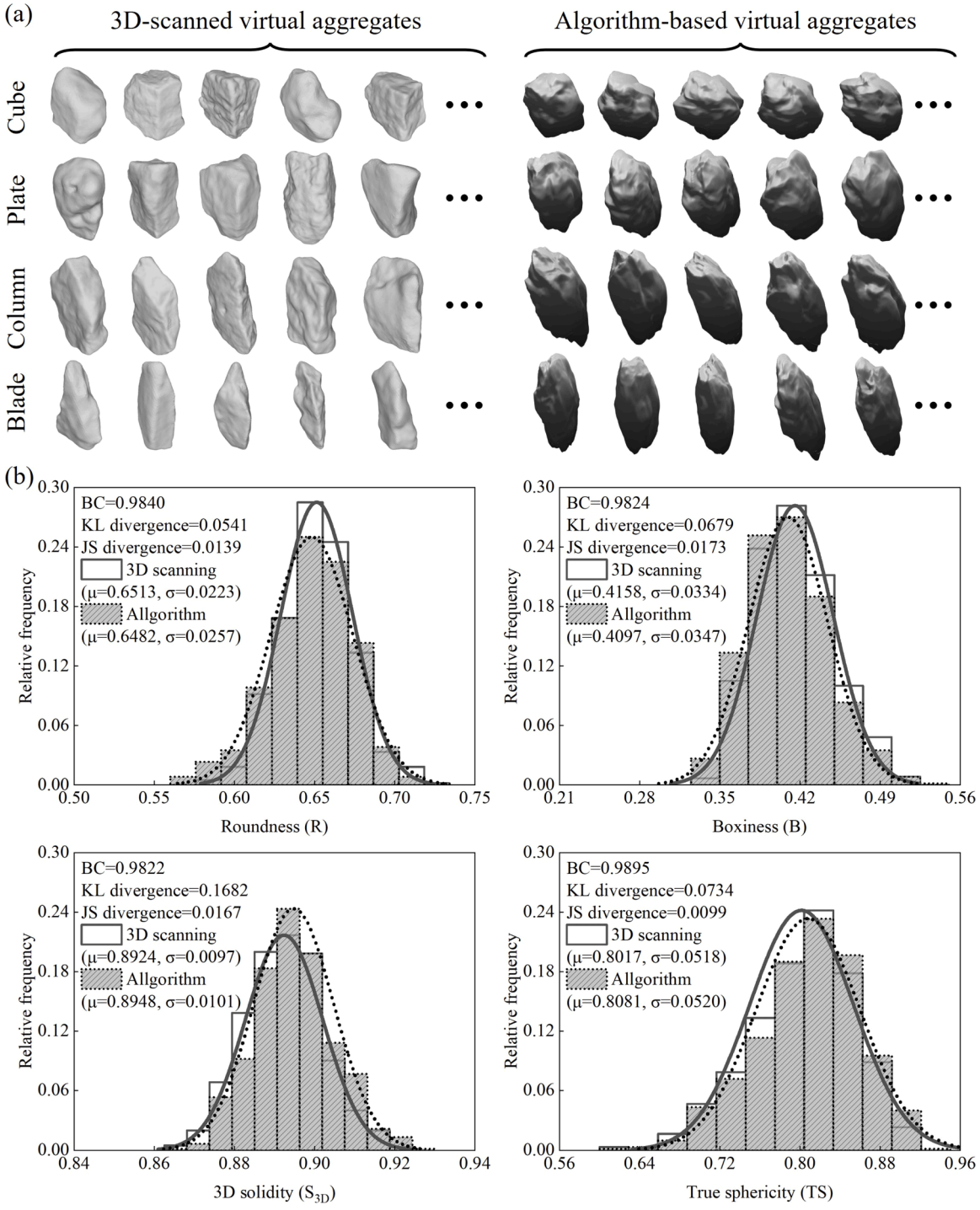

Fig. 8. Establishment of virtual aggregate databases: (a) comparison between 3D-scanned and algorithmic aggregate databases for four aggregate shapes, (b) distribution comparison of aggregate shape descriptor values.

Hünneberg, Germany. A total of 150 representative aggregates of each shape type are scanned, ultimately forming a validation database comprising 600 real aggregates. Subsequently, the algorithm generates 150 aggregates for each shape category (600 samples in total), in order to ensure comparability with the reference dataset. To improve the agreement between algorithm-generated virtual aggregates and the 3D-scanned aggregates, the model parameters are calibrated through a series of numerical experiments. Based on numerical testing, both s_w and s are set to 1, and [*L, W, H*] are drawn as random values constrained to satisfy the adopted shape classification criteria, while all other parameters are fixed to the benchmark values reported in Table 1. Fig. 8a displays representative samples from both databases. To further quantitatively investigate morphological differences in virtual aggregates across the two databases, statistical analysis is performed on the shape descriptor values of the samples.

The Bhattacharyya coefficient (BC) introduced by Bhattacharyya [69], the Kullback–Leibler (KL) divergence proposed by Kullback and Leibler [70], and the Jensen–Shannon (JS) divergence formulated by Lin [71] are three widely used statistical indices for quantifying similarity between probability distributions. A larger BC indicates a greater similarity between the two distributions, whereas smaller values of KL and JS divergences indicate greater similarity.

The BC is computed as:

$$BC(P,Q)=\sum_{x}\sqrt{P(x)Q(x)}. \tag{23}$$

The KL divergence is:

$$D_{KL}(P\parallel Q)=\sum_{x}p(x)\log\frac{p(x)}{q(x)}. \tag{24}$$

The JS divergence is then computed as:

$$D_{JS}(P,Q)=\frac{1}{2}D_{KL}(P\parallel M)+\frac{1}{2}D_{KL}(Q\parallel M), \tag{25}$$

where M is defined as an average distribution between P and Q:

$$M=\frac{1}{2}(P+Q), \tag{26}$$

where P and Q are probability distributions defined on a common sample space. Their corresponding probability mass or density functions are denoted by $p(x)$ and $q(x)$, respectively. The distribution M is a mixed distribution constructed from P and Q and is introduced to obtain a symmetrized form of the divergence. $BC(P, Q)$ measures the degree of overlap between two distributions P and Q. $D_{KL}(P\|Q)$ measures the information loss incurred when approximating P with Q, whereas $D_{JS}(P,Q)$ is defined as the average of the KL divergences from P and Q to M, serving to quantify the similarity between P and Q.

Based on the distributions of shape descriptor values for scanned aggregates and generated aggregates, the BC, KL divergence, and JS divergence are calculated, as shown in Fig. 8b The results demonstrate that the algorithm can faithfully reproduce the statistical morphological characteristics of real aggregates. The histograms of the four shape descriptors from the 3D-scanned database and from the algorithmic database largely overlap. Quantitatively, the BC exceeds 0.98 for all descriptors (0.9840 for R, 0.9824 for B, 0.9822 for S_{3D}, and 0.9895 for TS), confirming substantial distributional overlap. The JS divergences remain near 0.01–0.02 (0.0139, 0.0173, 0.0167, and 0.0099, respectively), while the KL divergences are modest, with the largest value observed for S_{3D} (0.1682) still indicating close similarity. Differences in the first two moments are small: for R the means are 0.6513 (scan) versus 0.6482 (algorithm) with comparable standard deviations (0.0223 vs 0.0257); for B the means are 0.4158 versus 0.4097 (0.0334 vs 0.0347); for S_{3D} the means are 0.8924 versus 0.8948 (0.0097 vs 0.0101); for TS the means are 0.8017 versus 0.8081 (0.0518 vs 0.0520). These deviations are within a narrow margin and show no systematic bias across descriptors or shape classes. Taken together, the high BC values, low KL and JS divergences, and close agreement of means and variances demonstrate that the proposed fractal-warped generation produces virtual aggregates whose morphological statistics are consistent with those of 3D-scanned aggregates, validating the algorithm as a reliable surrogate for generating high-fidelity aggregates.

A hypothesis-testing step is included to examine whether the discrepancies between the two databases can be attributed to random variation or indicate genuine differences. The shape descriptors from both databases are therefore subjected to an analysis of variance (ANOVA), with 0.05 adopted as the threshold for statistical significance. The corresponding analysis of variance results for the four shape descriptors are reported in Table 3. ANOVA demonstrates statistically significant differences between the two databases for all four descriptors at the 0.05 significance level. The strongest separation is observed for S_{3D} ($F = 17.8645$, $p = 2.55 \times 10^{-5}$), followed by B ($F = 9.6037$, $p = 1.99 \times 10^{-3}$). R ($F = 4.92$, $p = 0.0267$) and TS ($F = 4.6008$, $p = 0.0322$) are also significant, indicating detectable geometric disparities across indicators. However, statistical significance should be distinguished from practical significance. To complement the p-values, effect sizes (η^2) and confidence intervals are also reported in Table 3. The η^2 values remain small for all four descriptors (0.0041 for R, 0.0080 for B, 0.0150 for S_{3D}, and 0.0038 for TS), indicating that the between-database differences explain only a limited proportion of the total variance, even where statistical significance is detected. Likewise, the confidence intervals (CIs) of the group differences remain narrow, suggesting that the magnitude of the discrepancies is limited in practical terms. These minor discrepancies may arise from several factors, including the limited idealization of natural aggregates by the procedural generator, residual measurement uncertainty and mesh-reconstruction error in the 3D-scanned models, and the fact that real aggregates may contain irregular geological features that are only partially captured by the adopted descriptor-controlled parameterization. These results suggest that volumetric compactness and enclosure efficiency differ most clearly between databases, while corner rounding and overall sphericity vary more subtly. In particular, descriptors such as S_{3D} and B are more sensitive to small differences in concavity, local protrusions, and boundary enclosure, which may explain why they show relatively clearer separation between the two datasets. In subsequent studies, S_{3D} can serve as the primary discriminator, with B providing corroboration, while R and TS serve as supporting indicators for morphological changes at finer scales.

To provide a more nuanced evaluation beyond the pooled-sample comparison, additional category-wise analyses were performed for roundness (R) and true sphericity (TS), since these two descriptors are closely related to corner rounding and overall shape smoothness and are therefore suitable for examining shape-dependent fidelity. For R, the distributions for cube, plate, column, and blade particles are compared in Fig. 9, and the corresponding ANOVA results are summarized in Table 4. Overall, substantial overlap is still observed between the 3D-scanned and algorithm-generated datasets for all four particle-shape categories, indicating that the proposed generator preserves the roundness characteristics within each shape class. The best agreement is obtained for the plate category, with the highest BC (0.9867) and the lowest KL and JS divergences (0.0529 and 0.0132, respectively), while the cube, column, and blade categories also show high similarity, with BC values of 0.9537, 0.9652, and 0.9615. The mean values remain close within each category: the algorithm slightly underestimates R for cube and plate, but slightly overestimates it for column and blade, and the corresponding standard deviations are of similar magnitude in all cases. Although ANOVA indicates statistically significant differences for each category ($p < 0.05$), the associated effect sizes remain very small to small ($\eta^2 = 0.0013 - 0.0174$), and the confidence intervals are narrow, suggesting that the detected differences are limited in practical terms. Taken together, these shape-wise results support the same conclusion as the pooled analysis: the proposed algorithm reproduces the roundness

Table 3
Analysis of variance for the four shape descriptor values of sample data for the 3D-scanned aggregate database and the algorithmically generated aggregate database.

Shape descriptor	Source	Degrees of freedom	Sum of squares	Mean square	F-value	P-value	η^2	CI	Significant
Roundness (*R*)	Groups	1	0.002851	0.002851	4.92	0.02673	0.0041	0.000356–0.00581	**Yes**
	Error	1198	0.6943	0.0005796					
	Total	1199	0.6972	0.0005815					
Boxiness (*B*)	Groups	1	0.01114	0.01114	9.6037	0.001987	0.008	0.002236–0.009952	**Yes**
	Error	1198	1.3898	0.00116					
	Total	1199	1.4009	0.001168					
3D solidity (S_{3D})	Groups	1	0.001725	0.001725	17.8645	0.00002552	0.015	0.001285–0.003511	**Yes**
	Error	1198	0.1157	0.00009657					
	Total	1199	0.1174	0.00009793					
True sphericity (*TS*)	Groups	1	0.01239	0.01239	4.6008	0.03216	0.0038	0.0005492–0.0123	**Yes**
	Error	1198	3.2258	0.002693					
	Total	1199	3.2381	0.002701					

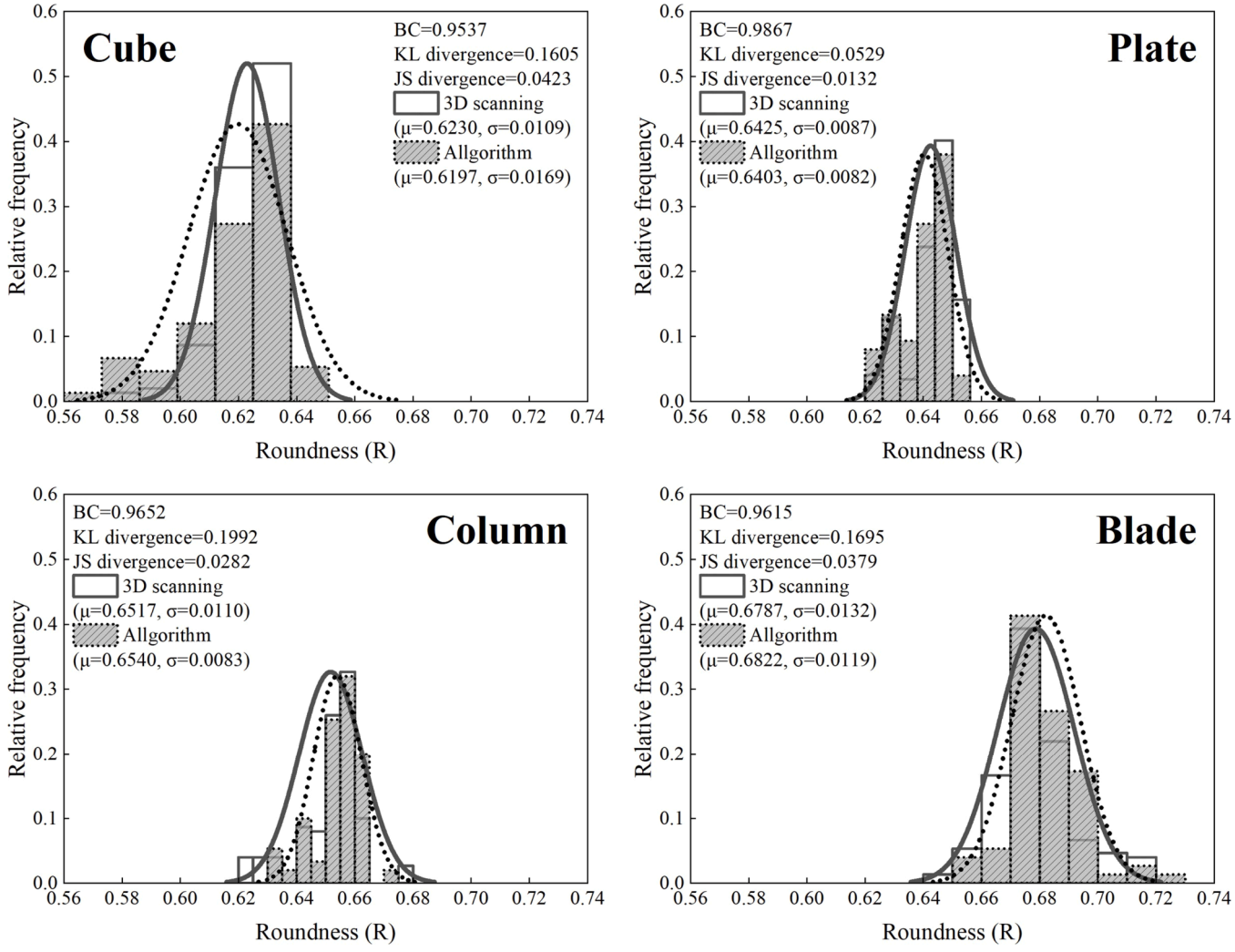

Fig. 9. Comparison of the value distribution of roundness (***R***) for different aggregate shapes.

distribution of scanned aggregates with good fidelity, while minor category-dependent deviations still remain.

A similar category-wise comparison was also carried out for true sphericity (*TS*), as shown in Fig. 10, with the corresponding ANOVA results listed in Table 5. In general, the scanned and algorithm-generated distributions still exhibit substantial overlap for all four particle-shape categories, indicating good shape-wise agreement in overall sphericity. Among them, the column particles show the strongest agreement, with the highest BC (0.9846) and the lowest KL divergence (0.0610), while cube, plate, and blade also maintain high distributional similarity, with BC values of 0.9640, 0.9595, and 0.9462, respectively. Compared with the scanned data, the algorithm-generated aggregates show a slight but consistent increase in mean *TS* for all four categories, namely from 0.8414 to 0.8473 for cube, from 0.7783 to 0.7846 for plate, from 0.7573 to 0.7642 for column, and from 0.7307 to 0.7379 for blade, while the corresponding standard deviations remain comparable or slightly smaller. This suggests that the generated particles tend to be marginally smoother or more sphere-like than the scanned ones within

Table 4
Analysis of variance for the roundness (***R***) of sample data from the 3D-scanned aggregate database and the algorithm-generated aggregate database based on different particle shapes.

Particle shape	Source	Degrees of freedom	Sum of squares	Mean square	F-value	P-value	η^2	CI	Significant
Cube	Groups	1	0.0007956	0.0007956	3.9231	0.04855	0.0013	0.00002094–0.006493	**Yes**
	Error	298	0.06043	0.0002028					
	Total	299	0.06123	0.0002048					
Plate	Groups	1	0.000364	0.000364	5.056	0.02527	0.017	0.0002749–0.004131	**Yes**
	Error	298	0.02145	0.00007199					
	Total	299	0.02182	0.00007297					
Column	Groups	1	0.0003892	0.0003892	4.0953	0.04389	0.0014	0.00006273–0.004493	**Yes**
	Error	298	0.02832	0.00009504					
	Total	299	0.02871	0.00009602					
Blade	Groups	1	0.0009083	0.0009083	5.7151	0.01744	0.0174	0.0006153–0.006345	**Yes**
	Error	298	0.04736	0.0001589					
	Total	299	0.04827	0.0001614					

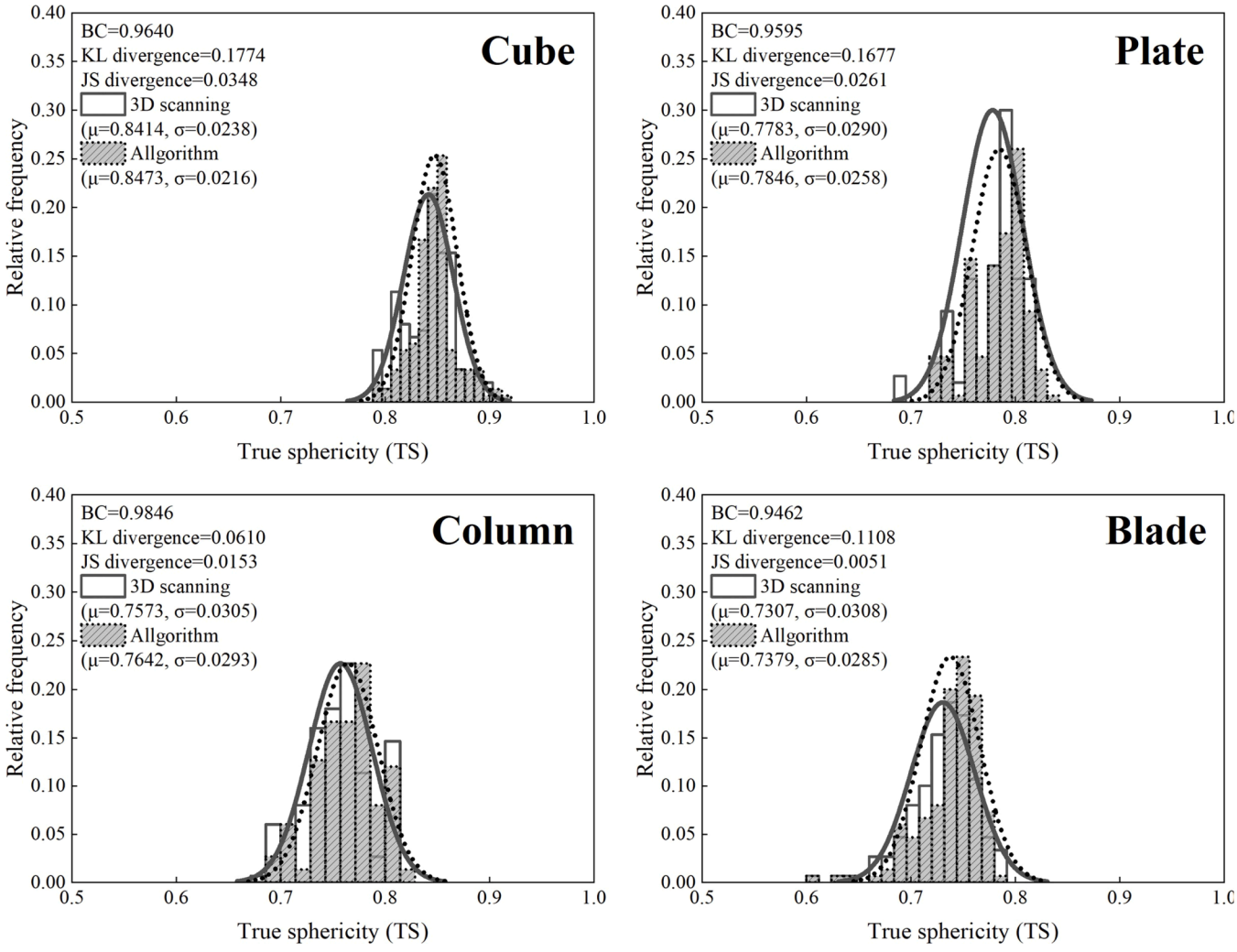

Fig. 10. Comparison of the value distribution of true sphericity (***TS***) for different aggregate shapes.

each shape class. Although ANOVA again indicates statistically significant differences for all categories ($p < 0.05$), the associated effect sizes remain small ($\eta^2 = 0.013 - 0.017$), and the confidence intervals are narrow, showing that the magnitude of these differences is limited. Overall, the category-wise results for *TS* confirm that the proposed algorithm reproduces the true sphericity characteristics of different aggregate shapes with good fidelity, while retaining only slight systematic deviations at the shape-class level.

6. Discrete element simulation of Superpave gyratory compaction

This section evaluates whether the proposed virtual aggregates can reproduce mixture-scale compaction behavior when used in particle-based numerical modeling. The practical usefulness of the algorithm-based aggregate database is examined by subjecting it to SGC simulations within a discrete element method (DEM) algorithm. SGC is adopted

Table 5
Analysis of variance for the true sphericity (*TS*) of sample data from the 3D-scanned aggregate database and the algorithm-generated aggregate database based on different particle shapes.

Particle shape	Source	Degrees of freedom	Sum of squares	Mean square	F-value	P-value	η^2	CI	Significant
Cube	Groups	1	0.002619	0.002619	5.0687	0.02509	0.017	0.0007439–0.01107	**Yes**
	Error	298	0.154	0.0005166					
	Total	299	0.1566	0.0005237					
Plate	Groups	1	0.003034	0.003034	4.0267	0.04569	0.013	0.0001227–0.0126	**Yes**
	Error	298	0.2245	0.0007534					
	Total	299	0.2275	0.000761					
Column	Groups	1	0.003591	0.003591	4.0174	0.04594	0.013	0.0001256–0.01371	**Yes**
	Error	298	0.2664	0.000894					
	Total	299	0.27	0.000903					
Blade	Groups	1	0.003878	0.003878	4.4033	0.03671	0.015	0.000447–0.01393	**Yes**
	Error	298	0.2625	0.0008808					
	Total	299	0.2663	0.0008908					

as a representative densification process because it couples confinement pressure and cyclic shear, making the response sensitive to particle interlocking, surface texture, and overall shape. Two simulation sets are constructed using aggregates from the 3D-scanned database and from the algorithm-generated database under matched gradation and specimen preparation procedures. Previous studies on SGC have shown that the compaction response of asphalt mixtures is strongly influenced by aggregate morphology, internal structure evolution, and particle-scale interaction mechanisms [72,73]. Existing experimental and numerical investigations have therefore widely used SGC as a representative approach for examining densification behavior, specimen-height evolution, and the role of aggregate characteristics during mixture compaction [74,75]. Subsequent content details the DEM setup, boundary and loading conditions, and contact parameter selection, followed by a comparative analysis of packing density evolution and gyration versus specimen height responses to assess engineering consistency between the two aggregate sources.

The previous analysis concentrated on the sensitivity of the control parameters and on how faithfully the virtual aggregates reproduce real morphology. A further key issue is whether the algorithm-generated aggregates enable predictions of asphalt mixture mechanical responses that are both more accurate and more robust. To investigate this, both the 3D-scanned reference database and the algorithm-generated database are implemented within an identical DEM framework, so that the impact of the algorithm on mixture-scale behavior can be examined in a systematic way. DEM, originally developed by Cundall and Strack [76], represents granular media as assemblies of discrete particles. Each particle moves according to Newtonian mechanics. Contact models are employed to evaluate particle–particle interactions as well as particle–boundary interactions, thereby reproducing the packing structure along with the associated load transfer mechanisms. To simulate the interactions between aggregate particles coated with an asphalt film, the Johnson–Kendall–Roberts (JKR) contact model [77] is adopted (Fig. 11a). This model has been widely validated for representing adhesion arising from van der Waals forces between materials [78–81]. The aggregate gradation used in the SGC simulations is shown in Fig. 11b The interpretation of the JKR formulation and the associated parameter settings follows prior studies [36,82], with detailed information provided in Appendix C.

First, an aggregate packing simulation generates a loose asphalt mixture to examine how algorithm-generated aggregates affect the packing structure (Fig. 11c). A total of 9000 aggregate particles are first placed at random inside a rigid confinement domain and then left to move under self-weight until a mechanically stable configuration is obtained. A rigid platen then applies a nominal stress of 600 kPa to precompact the assembly until the specimen height reaches 70 mm. Through this procedure, the internal mesostructure of the assembly is characterized, capturing particle orientations, the spatial distribution of voids, and the network of contacts between particles. After the precompaction stage, the packing density (PD) is then used to express the aggregate volume fraction within the packing system as:

$$PD = \frac{V_{Aggregate}}{V_{Container}}, \tag{27}$$

where $V_{Aggregate}$ represents the overall volume occupied by the aggregates, and $V_{Container}$ represents the volume of the container that holds them.

SGC simulations are subsequently carried out on the loose asphalt mixture model to replicate the laboratory compaction procedure applied to asphalt mixtures. The corresponding numerical setup is depicted in Fig. 11d The unconsolidated mixture is introduced into a cylindrical mold, which is constrained by rigid platens at its top and bottom surfaces. During the compaction stage, the mold is driven in a prescribed gyratory motion at a constant tilt angle of 0.82° and a rotation speed of 30 rpm. The lower platen is kept fixed, whereas the upper platen applies a constant vertical stress of 600 kPa until the specimen height is reduced to 63.5 mm. In this configuration, the simulation resolves aggregate rearrangement, the associated transfer of loads, and the evolution of air voids over the entire compaction history. As a result, it becomes possible to make a detailed comparison of the mechanical responses of mixture models constructed from the two different aggregate databases. During the entire simulation, the PD and the relationship between gyration number and specimen height are monitored. The resulting gyration–height curve is subsequently approximated by the following function:

$$H = AG^{B}, \tag{28}$$

where H denotes the specimen height, G is the corresponding number of gyrations, and A and B are the curve-fitting parameters.

To control random variability in numerical experiments, six cases of SGC simulations are performed. Each case includes one run using 3D-scanned aggregates and three runs using algorithmically generated aggregates, with distinct aggregate shapes employed across each set. Fig. 12a presents the PD results for the loose asphalt mixture, while Fig. 12b shows those for the compacted asphalt mixture.

Fig. 12a shows that the PD of the loose mixtures produced from the algorithm-based particles is essentially indistinguishable from that of the 3D-scanned aggregates across all six cases. The observed PD values fall within a narrow band of approximately 52.3–53.6%, with case-by-case differences between the two databases generally below one percentage point. The algorithm-based assemblies exhibit a slightly higher mean PD in several cases, but the spread is small and the overlap across cases is substantial, indicating comparable initial packing structures.

After gyratory compaction, Fig. 12b indicates a systematic increase in PD to roughly 57.4–58.5% for both databases. The two sets remain closely aligned for every case, and the case-to-case variability stays low, which suggests that the compaction pathway and resultant densification are governed by similar rearrangement and contact formation mechanisms irrespective of the database used. Taken together, the loose and

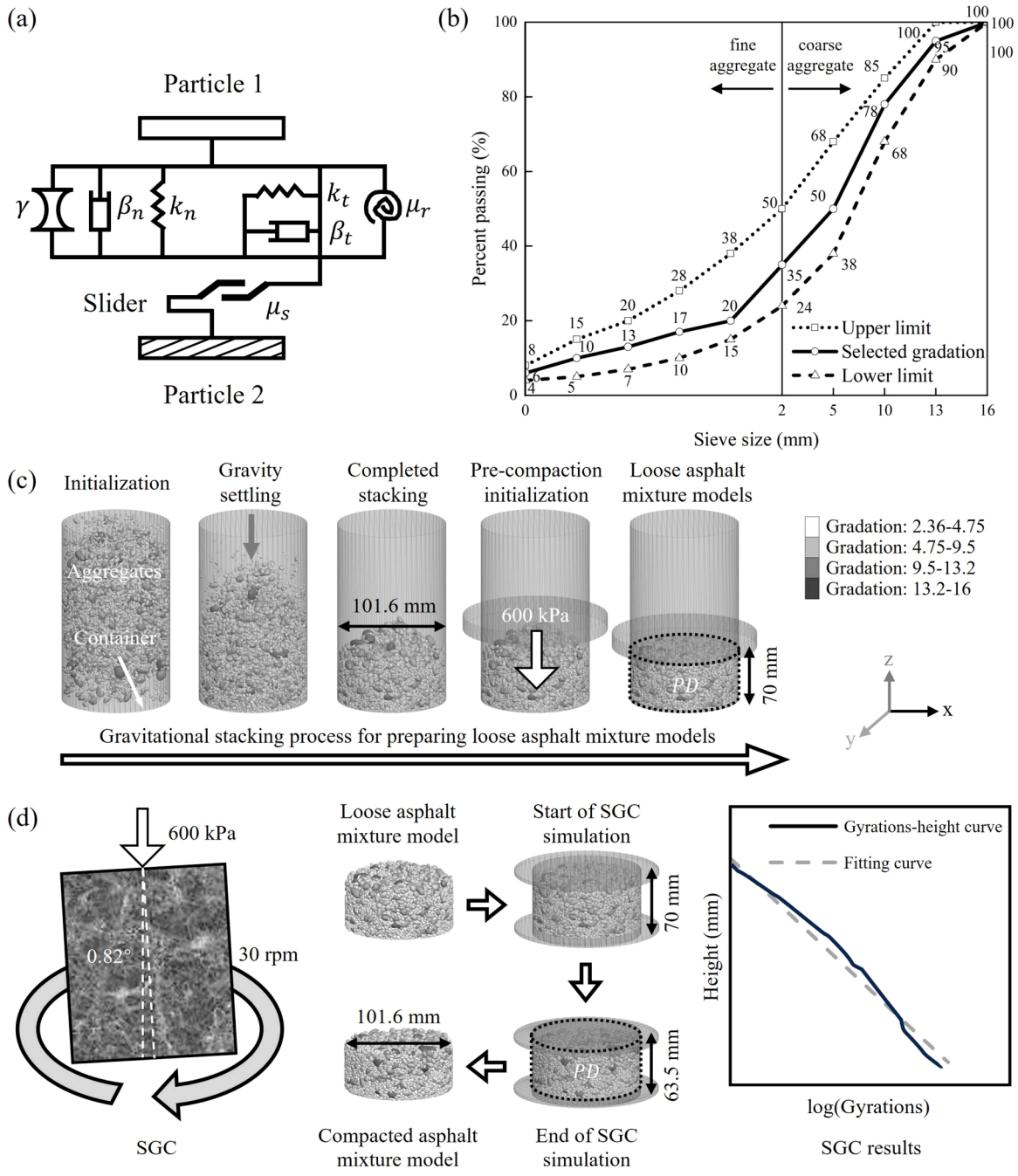

Fig. 11. Superpave gyratory compaction (SGC) simulation: (a) Johnson–Kendall–Roberts (JKR) contact model, (b) schematic diagram of the particle size distribution curve for aggregate using AC-13 gradation, (c) production of loose asphalt mixtures based on DEM, (d) SGC simulation process based on DEM and results testing schematic.

compacted states demonstrate that the algorithm-generated aggregates reproduce mixture-level packing metrics with high fidelity relative to 3D-scanned counterparts, both before and after SGC densification.

Fig. 13 shows the gyration–height relationships derived from the SGC simulations. The corresponding curve-fitting expressions and their coefficients of determination are reported in Table 6. Across the six simulated cases, the gyration–height curves for mixtures constructed from 3D-scanned aggregates are almost indistinguishable from those for the three mixtures constructed from algorithm-generated aggregates in each case. No systematic deviation is observed over the entire logarithmic gyration range. Power-law fits of the form $H = AG^B$ yield prefactors A clustered around 70.2–70.4 mm and exponents B tightly concentrated near -2.9×10^{-2}. Case-to-case variations of A are within about one percent and differences in B are on the order of 10^{-3}. The goodness of fit remains consistently high, with coefficients of determination exceeding 0.99 in all instances, indicating that both databases reproduce the same compaction trajectory. Combined with the PD results, these gyration–height curves demonstrate that the aggregate database generated by the algorithm is able to replicate, with high fidelity, the macroscopic compaction behavior of mixtures made with real aggregates.

7. Limitations

The proposed generator is based on a star-shaped radial-graph representation, in which the particle surface is described by a single-valued

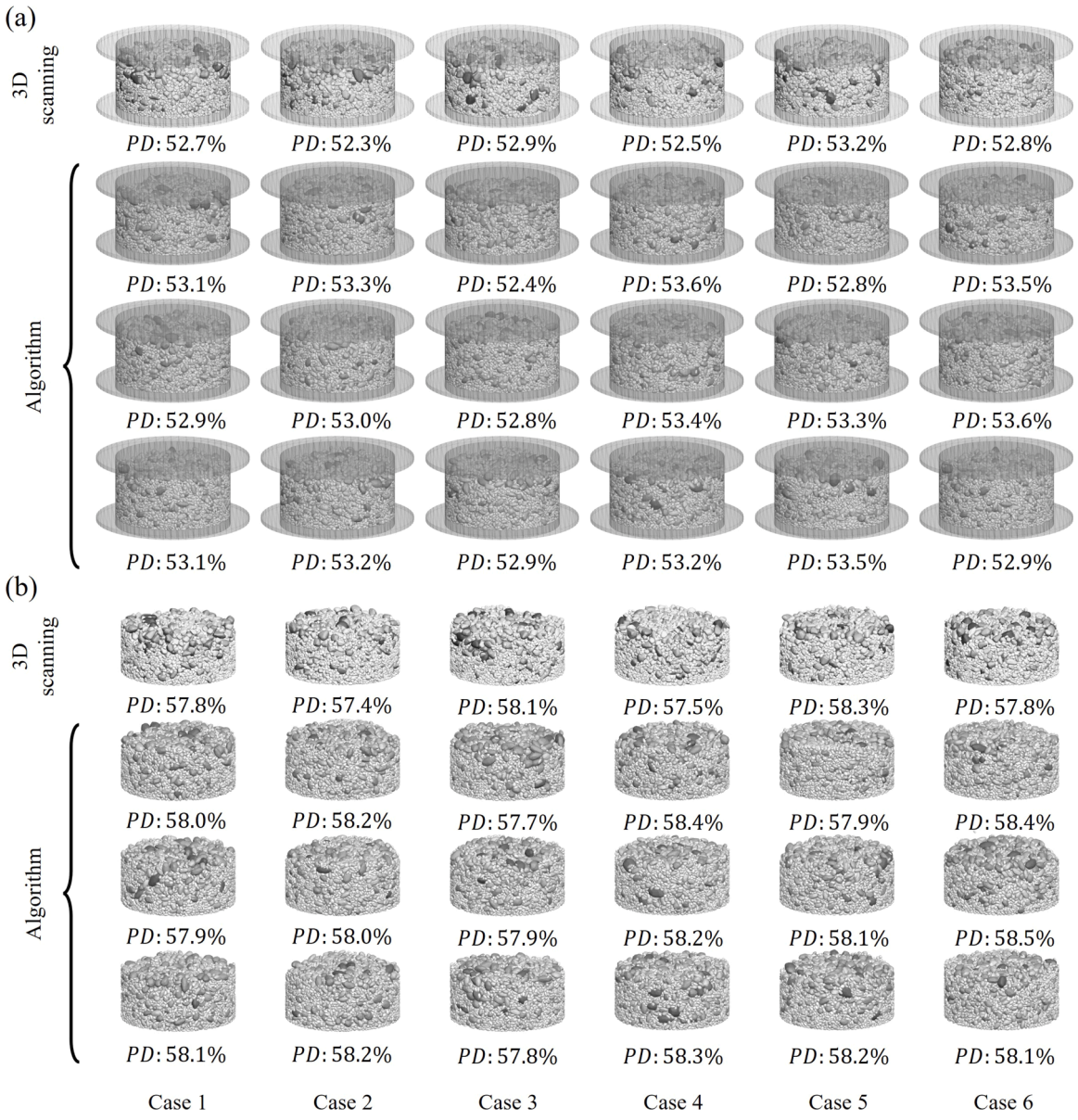

Fig. 12. Aggregate packing density in asphalt mixture models: (a) generation of loose asphalt mixtures using 3D-scanned virtual aggregates and algorithmically generated virtual aggregates, (b) generation of compacted asphalt mixtures using 3D-scanned virtual aggregates and algorithmically generated virtual aggregates.

radius function on the unit sphere. This representation is well suited to irregular but predominantly star-shaped and near-convex aggregates, which are common in the compaction scenarios considered in this study. However, its geometric expressiveness is inherently bounded. In particular, the formulation assumes that each ray emitted from the reference origin intersects the surface only once. As a result, the present method is not able to explicitly represent re-entrant features, internal voids, strongly overhanging geometries, or highly non-star-shaped particles with multiple radial intersections. When such morphologies occur, the algorithm may smooth, suppress, or geometrically regularize these features rather than reproduce them faithfully. For this reason, the proposed representation should be understood as most applicable to aggregates whose morphology can be reasonably approximated as a star-shaped irregular body, rather than as a universal model for all possible rock-fragment geometries.

A related limitation is that, although the generated database reproduces the central tendency of the scanned population well, the current parameterization may still underrepresent particles located at the tails of the shape distribution. This is particularly relevant for aggregates with extreme angularity, pronounced flatness, or large aspect ratio, which may arise from specific lithologies or unconventional crushing processes. Such tail morphologies are important because they can exert disproportionate influence on packing density, interlocking, and segregation behavior. In the present study, the proposed algorithm is therefore best interpreted as a controllable and simulation-ready generator for the dominant morphological regime of engineering aggregates, rather than a complete descriptor of all extreme particle forms. Future work could extend the geometric applicability of the framework by integrating complementary representations, such as signed distance field (SDF)-based implicit surfaces, hybrid local concavity embedding, or convex-hull-perturbation strategies, so that both typical particles and distributional extremes can be represented within a broader unified framework.

8. Conclusion

This study develops a novel algorithm that automatically generates virtual aggregates and evaluates their morphological fidelity as well as

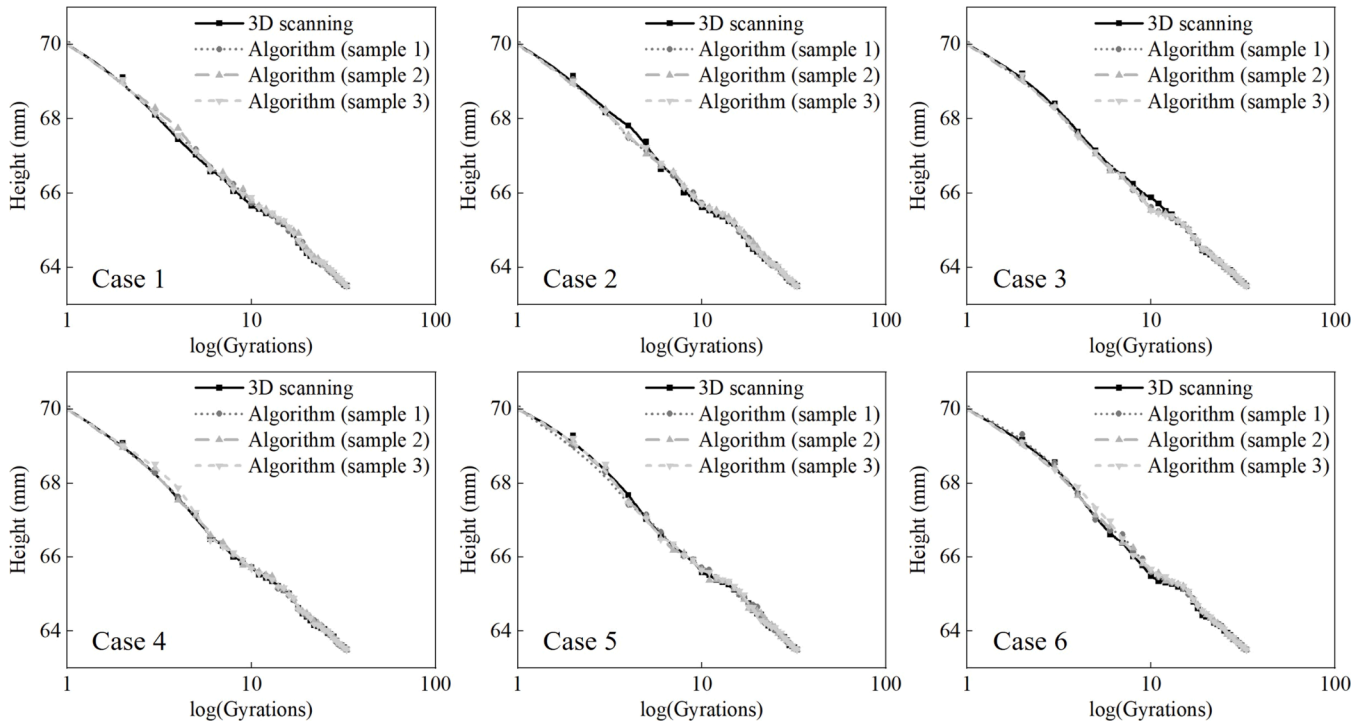

Fig. 13. Simulation results of SGC for six different cases regarding the gyration-height curve.

Table 6
Curve fitting of gyration–height relationships for six different cases.

Case number	3D scanning	Algorithm (sample 1)	Algorithm (sample 2)	Algorithm (sample 3)
1	$H = 70.2147G^{-0.0286}$ $R^2 = 0.9961$	$H = 70.2923G^{-0.0288}$ $R^2 = 0.9968$	$H = 70.3315G^{-0.0288}$ $R^2 = 0.9953$	$H = 70.2563G^{-0.0285}$ $R^2 = 0.9959$
2	$H = 70.3466G^{-0.0292}$ $R^2 = 0.9944$	$H = 70.2953G^{-0.0288}$ $R^2 = 0.9966$	$H = 70.2147G^{-0.0286}$ $R^2 = 0.9961$	$H = 70.2916G^{-0.0287}$ $R^2 = 0.9968$
3	$H = 70.4046G^{-0.0293}$ $R^2 = 0.9955$	$H = 70.2816G^{-0.0289}$ $R^2 = 0.9960$	$H = 70.2718G^{-0.0288}$ $R^2 = 0.9956$	$H = 70.2821G^{-0.0288}$ $R^2 = 0.9953$
4	$H = 70.2622G^{-0.0289}$ $R^2 = 0.9953$	$H = 70.2762G^{-0.0289}$ $R^2 = 0.9967$	$H = 70.2687G^{-0.0287}$ $R^2 = 0.9955$	$H = 70.3451G^{-0.0291}$ $R^2 = 0.9927$
5	$H = 70.3231G^{-0.0290}$ $R^2 = 0.9940$	$H = 70.2463G^{-0.0286}$ $R^2 = 0.9953$	$H = 70.2644G^{-0.0288}$ $R^2 = 0.9930$	$H = 70.3105G^{-0.0289}$ $R^2 = 0.9918$
6	$H = 70.3283G^{-0.0292}$ $R^2 = 0.9920$	$H = 70.4271G^{-0.0295}$ $R^2 = 0.9932$	$H = 70.3520G^{-0.0291}$ $R^2 = 0.9950$	$H = 70.4287G^{-0.0294}$ $R^2 = 0.9937$

their simulation performance relative to 3D-scanned aggregates. The approach blends a domain-warped multifractal implicit-radius field with practical mesh processing and descriptor-based calibration, enabling targeted control of roughness, ridges, chipping, and anisotropy while preserving watertightness for downstream computation. The main outcomes of this research can be outlined as follows:

1. The proposed algorithm, built on a warped multifractal field that mixes fractional Brownian motion (FBM), ridged multifractals, and Worley-type chipping with layered anisotropy, produces watertight meshes whose macro-dimensions are decoupled from micro-texture and whose parameters map transparently to interpretable morphology controls. In addition to the field construction, the pipeline integrates simulation-oriented operations (PCA/AABB dimensional calibration, optional twist, light smoothing, and bottom capping), providing a direct path from stochastic synthesis to numerically robust, placement-ready particle meshes without sacrificing multi-scale surface realism.
2. A calibration protocol grounded in four standard shape descriptors (roundness R, boxiness B, 3D solidity S_{3D}, and true sphericity TS) quantifies sensitivity to control parameters and supports resolution choices; among descriptors, B remains essentially invariant to mesh decimation, whereas R is the most sensitive to parameter changes. The sensitivity separation across $\{R, B, S_{3D}, TS\}$ offers a practical guideline for targeted tuning: parameters governing roughness amplitude and multi-scale content primarily affect corner curvature and convexity-related measures, while volume-enclosure measures are comparatively stable, improving interpretability and reproducibility in parametric studies.
3. Against a 3D-scanned reference database, the generated database achieves close distributional alignment in descriptor statistics and shows small but statistically detectable differences in hypothesis testing at the dataset level. This indicates high morphological fidelity suitable for numerical studies, while also suggesting that subtle residual discrepancies can persist at the population scale. Such differences are sufficiently small to preserve practical representativeness, and they can be further reduced through descriptor-targeted parameter refinement when strict statistical matching is required.
4. Within a consistent discrete element method (DEM) framework, mixture models assembled from generated aggregates reproduce

packing density and gyration–height responses observed for scanned aggregates, with tight case-to-case variability and excellent curve fits. This agreement demonstrates that the generated particle geometry preserves mixture-scale mechanical behavior in the Superpave gyratory compaction (SGC) setting, supporting the engineering relevance of the proposed generator beyond purely geometric similarity.

Overall, the results indicate that the algorithm delivers controllable, physics-plausible, and validated virtual aggregates that are ready for simulation, providing reliable, reproducible, and scalable inputs for numerical analyses in civil and pavement engineering. The algorithm reduces reliance on labor-intensive scanning when large virtual populations are needed, and it enables systematic investigations into how specific morphological traits influence compaction and packing outcomes under controlled conditions. In future applications, the proposed algorithm can be extended to the development of multiscale numerical models for asphalt mixtures, granular geomaterials, and other particulate civil-engineering systems in which particle morphology plays a governing mechanical role. It also provides a practical foundation for high-throughput parametric studies, virtual material design, and morphology-informed performance optimization in road and infrastructure engineering.

Data availability

The source code implementing the proposed virtual aggregate generation algorithm has been released as open-source and is hosted on GitHub. The link is as follows: https://github.com/ffd960131/Aggregate-generation-algorithm.

CRediT authorship contribution statement

Dong Feng: Writing – review & editing, Writing – original draft, Visualization, Validation, Software, Resources, Project administration, Methodology, Investigation, Funding acquisition, Formal analysis, Data curation, Conceptualization.

Declaration of competing interest

The author declares that he has no known competing financial interests or personal relationships that could have appeared to influence the work reported in this paper.

Acknowledgements

Funding for this study is provided by the China Scholarship Council (CSC) under Grant No 202308080042. The author also wishes to thank three anonymous reviewers and the editor for their valuable comments on earlier versions of this paper.

Appendix A. Detailed parameter calibration workflow and one-at-a-time (OAT) sampling protocol

The descriptor-driven calibration adopted in this study was carried out in two stages. The first stage aimed to establish a reproducible forward mapping between control parameters and shape descriptors through one-at-a-time (OAT) sensitivity analysis. The second stage used the resulting insights to select a practical parameter setting for database generation and for the subsequent descriptor-targeted inverse validation. The purpose of this appendix is to document the full calibration workflow, including the parameter ranges, screening logic, treatment of random seeds, and the way common and shape-dependent settings were handled.

For the forward calibration reported in Section 4, the first 15 generative parameters were investigated, while the dimensional calibration strategy and twist parameter were treated separately in the analyses associated with Fig. 6. Each OAT curve was obtained by varying one parameter within a prescribed search range and keeping the remaining parameters at their benchmark values. At each sampling point, 30 random seeds were generated, and the four descriptor values, namely roundness R, boxiness B, 3D solidity S_{3D}, and true sphericity TS, were averaged to obtain the reported response value. This OAT design was intended to reveal first-order descriptor trends and to identify which parameters dominate roughness, convexity, and sphericity, rather than to fully characterize interaction effects in the complete high-dimensional space.

The search ranges used in the OAT study are summarized in Table 7. For most parameters, the sampling was performed on discrete linear grids over the indicated interval. The phase-offset parameter $\boldsymbol{\delta}_i$ was sampled symmetrically around zero in order to capture rephasing effects without changing the overall statistics of the field. The sharpness exponent κ spans several orders of magnitude and was therefore examined over a wide positive range, consistent with the nonlinear sharpening role discussed in the main text. These ranges correspond to the parameter domains explored in Fig. 6 and define the admissible screening space used for the descriptor-parameter mapping.

Table 7
Search ranges used in the OAT descriptor-parameter calibration.

Serial number	Symbol	Search range in Fig. 6	Sampling note
1	r	0 to 5	linear grid
2	k	0 to 1	linear grid
3	s	0 to 3	linear grid
4	s_w	0 to 3	linear grid
5	η	0 to 1	linear grid
6	$\boldsymbol{\delta}_i$	−6 to 6	symmetric grid
7	O	0 to 10	discrete integer-like sweep
8	λ	0 to 3	linear grid
9	g	0 to 1	linear grid
10	α	0 to 2	linear grid
11	β	0 to 1	linear grid
12	γ	0 to 2	linear grid
13	κ	0.1 to 128	wide positive sweep
14	A_L	0 to 8	linear grid
15	f_L	0 to 5	linear grid

No single scalar objective function was used in the OAT stage. Instead, the calibration operated as a numerical screening procedure. Parameters were assessed according to how strongly and consistently they influenced the descriptor set {*R, B, S_{3D},TS*}. In this framework, parameters such as *k, s, O*, λ, *g*, α, β, and γ were identified as the main morphology-governing controls, whereas *B* remained comparatively insensitive over much of the explored space. The practical interpretation of these trends was then used to guide subsequent parameter selection and inverse descriptor matching.

For the database-level calibration in Section 5, the objective was different from that of the OAT study. Instead of tracing local one-parameter trends, the aim was to obtain a single practical generator setting that could reproduce the overall morphology of the scanned aggregate population. Accordingly, the final database-level selection was based on numerical experiments and population-level comparison against the scanned reference database. The screening criteria were the agreement of descriptor distributions, the closeness of the first two moments, and the statistical consistency indicators reported in the main text, including the Bhattacharyya coefficient, Kullback-Leibler divergence, Jensen-Shannon divergence, and the subsequent hypothesis-testing results. In practical terms, preferred parameter settings were those that produced high overlap, small divergence values, and only limited practical discrepancies between the generated and scanned databases.

The treatment of random seeds followed the same logic throughout the study. In the OAT sensitivity analysis, multiple seeds were used at each sampling point and averaged in order to suppress seed-specific fluctuations and expose stable first-order trends. In the inverse validation and in the final database generation, independent random seeds were retained so that the generator could preserve realistic within-class variability. Therefore, the seed was not calibrated as a deterministic control variable, but treated as a stochastic source of particle-to-particle variation around a calibrated descriptor level.

The global texture-control parameters were unified across particles by keeping the calibrated benchmark-style setting for the common generator controls. Shape-class differentiation was then introduced through the dimensional constraints used to satisfy the adopted aggregate classification criteria, together with independent random seeds for individual particle realization. In other words, the underlying multifractal generator remained common, whereas the final particle population was diversified through class-dependent dimensional admissibility and stochastic realization. This choice was made to preserve a consistent generative style while still matching the cube, plate, column, and blade categories used in the validation database.

Finally, it should be noted that the OAT calibration reported in the main text was designed as a transparent and interpretable first-order screening framework. For this reason, it does not claim to resolve all parameter interactions in the full 15-dimensional space. To broaden the exploration beyond the OAT paths, the supplementary space-filling and inverse-search procedure reported in Appendix B was introduced as an additional practical tool for descriptor-oriented parameter identification and closed-loop validation.

Appendix B. Supplementary space-filling screening and inverse descriptor matching

To complement the OAT sensitivity analysis presented in the main text (see Section 4), a supplementary parameter-screening and inverse-matching procedure was established. The purpose of this procedure is not to replace a full global sensitivity analysis, but to provide a practical extension from the existing OAT results to subsequent tasks, including target descriptor specification, candidate parameter identification, aggregate regeneration, and descriptor re-evaluation. In this way, the procedure supplements the main methodology by transforming the previously obtained one-dimensional descriptor responses into a searchable multidimensional design library.

The starting point of the procedure is the set of discrete OAT response curves for the 15 control parameters of the generator (see Fig. 6). For each parameter, the corresponding responses of the four shape descriptors, namely roundness (*R*), boxiness (*B*), 3D solidity (S_{3D}), and true sphericity (*TS*), were available over a prescribed sampling range. Based on these data, a first-order surrogate model was constructed for each descriptor by interpolating the one-dimensional response of each parameter while all remaining parameters were kept at the baseline configuration. Let x_i denote the *i*-th parameter and $x_i^{(0)}$ its baseline value. For descriptor *d*, the predicted response at a sampled parameter vector $\mathbf{x} = (x_1,\cdots, x_{15})$ was approximated by the additive main-effects model:

$$\widehat{y}_d(\mathbf{x}) = y_d^{(0)} + \sum_{i=1}^{15}\left[f_{i,d}(x_i) - f_{i,d}\left(x_i^{(0)}\right)\right], \tag{29}$$

where $f_{i,d}(\cdot)$ is the interpolated OAT response of descriptor *d* with respect to parameter x_i, and $y_d^{(0)}$ is the baseline descriptor value. This construction preserves the main-effect trends identified in the OAT analysis while enabling efficient evaluation of multidimensional parameter combinations. Since the available information is OAT-based, interaction effects between parameters are not explicitly represented in this surrogate.

A Latin hypercube sampling (LHS) design was then used to generate a space-filling set of parameter combinations within the admissible ranges of the 15 control parameters. For each sampled point, the four descriptors were predicted using the additive surrogate. To identify candidate parameters for a prescribed target descriptor vector $\mathbf{y}^* = \left[R^*, B^*, S_{3D}^*, TS^*\right]$, a weighted normalized mismatch was defined as:

$$E(\mathbf{x}) = \left[\sum_{d=1}^{4}\left(w_d\frac{\widehat{y}_d(\mathbf{x}) - y_d^*}{t_d}\right)^2\right]^{\frac{1}{2}}, \tag{30}$$

where w_d is the weight assigned to descriptor *d*, and t_d is the tolerance associated with that descriptor. Smaller values of *E* indicate better agreement between the predicted descriptor vector and the target one. The sampled parameter combinations were ranked according to this weighted error, and the best candidates were retained for subsequent aggregate generation and verification. In parallel, a tolerance-based criterion was used to identify whether all four predicted descriptors simultaneously satisfied the prescribed admissible bands.

To facilitate interpretation of the sampled design space, an interactive three-dimensional graphical user interface (GUI) was further developed (see Fig. 14). The GUI allows the user to select any three quantities from the descriptor set {*R, B, S_{3D},TS*}, the generator parameter set, and the weighted mismatch *E*, and to display them along the *x*-, *y*-, and *z*-axes, respectively. The sampled point cloud is colored by *E*, so that regions associated with

better descriptor matching can be visually identified. The interface also allows the best-ranked candidates to be highlighted and the target or baseline point to be displayed for reference. In addition, data tips provide direct access to the numerical values of descriptors, parameter settings, and matching error for any selected sample. This GUI therefore serves as a practical exploratory tool for linking descriptor space and parameter space.

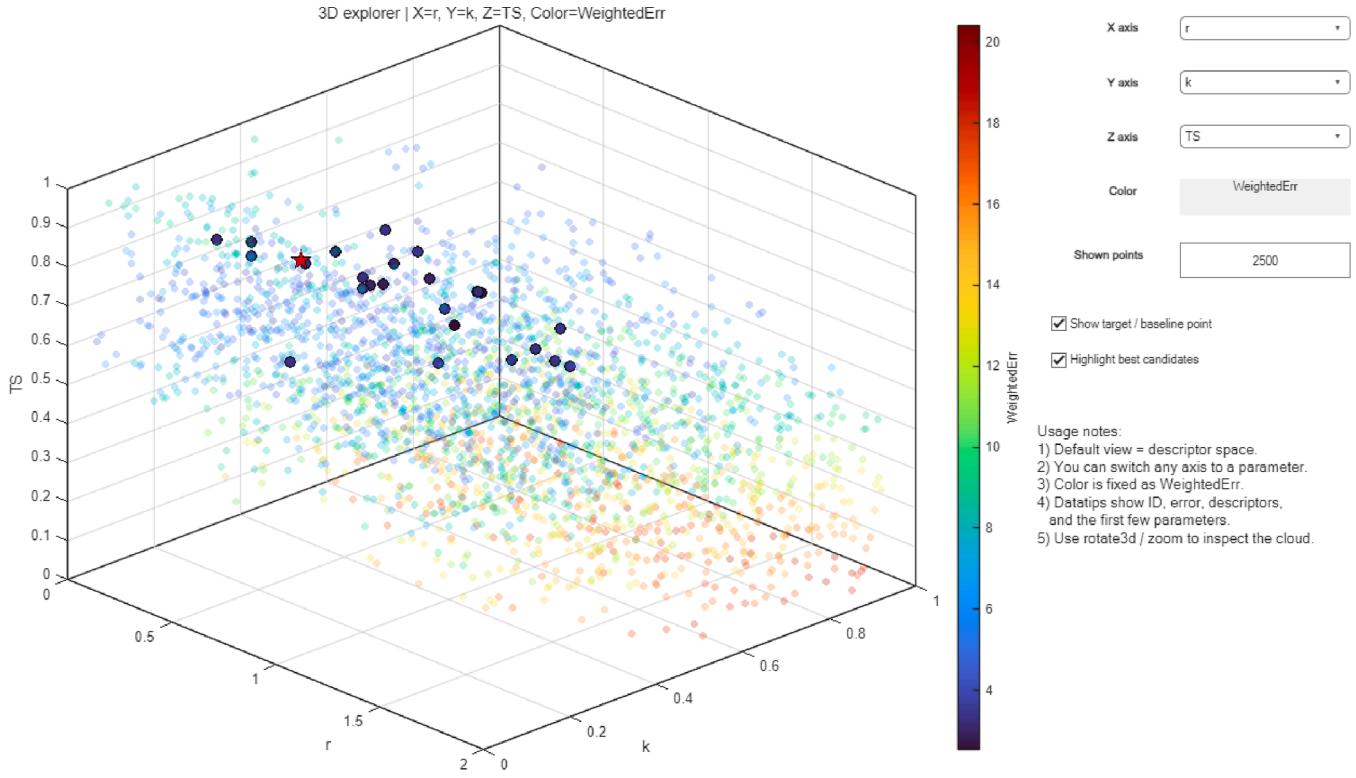

Fig. 14. Main interface of the interactive 3D design explorer for space-filling parameter screening and inverse descriptor matching.

The outputs of the procedure include the sampled multidimensional design library, the ranked list of candidate parameter vectors, and the associated predicted descriptor values. These results supplement the main text by providing a reproducible descriptor-oriented screening framework that supports parameter inversion and subsequent validation. At the same time, the present workflow remains a first-order approximation derived from OAT data. Therefore, it should be regarded as a practical screening and inverse-search tool rather than a full interaction-aware global sensitivity framework. If a more rigorous characterization of the complete high-dimensional parameter space is required in future work, this procedure could be extended by incorporating dedicated space-filling simulations, interaction-aware surrogate models, and variance-based global sensitivity measures.

Appendix C. DEM particle representation, contact detection, and contact-model parameters

In the DEM simulations, both the 3D-scanned aggregates and the algorithm-generated aggregates were represented directly as rigid blocks imported from their watertight triangulated surface meshes. No sphere-clump approximation, polyhedral replacement, or additional mesh simplification was introduced during DEM implementation. Therefore, the particle geometry used in the DEM calculations remained consistent with the geometry obtained after the mesh-processing steps described in the main text. This choice was made to preserve the shape details that are important for particle interlocking and compaction response, while ensuring that the comparison between the scanned and generated databases was conducted within the same geometric representation framework.

Contact detection between rigid blocks was performed using the Gilbert–Johnson–Keerthi (GJK) algorithm [83]. Once a contact pair was identified, the local interaction was resolved using the JKR contact model with tangential resistance and rolling friction. The same particle representation, contact detection approach, and contact law were used for both the scanned and algorithm-generated particles, so that the DEM comparison in Section 6 reflected differences in particle morphology under a common numerical framework.

Table 8 summarizes the force and moment formulas for the JKR contact model. Table 9 describes the meaning of each parameter. For reproducibility, the complete set of DEM input parameters used in the SGC simulations is explicitly listed in Table 10. These parameters were adopted based on the authors' previous research [8,36]. Because the particles were treated as rigid blocks, the DEM model did not account for particle breakage or bulk deformation of the aggregates. Mechanical compliance was introduced only through the local contact law. In addition, the direct use of unsimplified triangulated particle geometry improved geometric fidelity, but it also increased computational cost compared with simplified sphere-based or reduced-geometry representations. These numerical approximations should be kept in mind when interpreting the DEM results. However, they were applied equally to both databases and therefore do not affect the internal consistency of the comparative validation presented in this study.

Table 8
Force and moment formulas for the Johnson–Kendall–Roberts (JKR) contact model.

Normal force	Contact	$\overline{F}_n^e = \frac{4E_{ij}\overline{a}^3}{3r_{ij}} - \sqrt{16\pi\gamma E_{ij}\overline{a}^3}$, (31)
		where the analytic solution for $\overline{a}$ as a function of $\overline{\delta}_n$ is determined according to [84].
	Damping	$\overline{F}_n^d = -2\beta_n\overline{u}_n^{rel}\sqrt{\overline{S}_n m_{ij}}$. (32)
Tangential force	Contact	$\overline{F}_t^e = \begin{cases} \overline{S}_t\overline{\delta}_t, & \|\overline{S}_t\overline{\delta}_t\| \le \lvert\mu_s(\overline{F}_n^e + 6\pi\gamma r_{ij})\rvert \\ \mu_s(\overline{F}_n^e + 6\pi\gamma r_{ij}), & otherwise \end{cases}$. (33)
	Damping	$\overline{F}_t^d = -2\beta_t\overline{u}_t^{rel}\sqrt{\overline{S}_t m_{ij}}$. (34)
Moment	Rolling friction	$\overline{M}^r = \begin{cases} -\overline{S}_t r_{ij}^2\overline{\theta}^{rel}, & \|\overline{M}^r\| \le \lvert\mu_r r_{ij}(\overline{F}_n^e + 6\pi\gamma r_{ij})\rvert \\ \mu_r r_{ij}(\overline{F}_n^e + 6\pi\gamma r_{ij}), & otherwise \end{cases}$. (35)

with $E_{ij} = \left(\frac{(1-\nu_i^2)}{E_i} + \frac{(1-\nu_j^2)}{E_j}\right)^{-1}$, (36)

$r_{ij} = \left(\frac{1}{r_i} + \frac{1}{r_j}\right)^{-1}$, (37)

$m_{ij} = \left(\frac{1}{m_i} + \frac{1}{m_j}\right)^{-1}$, (38)

$\overline{S}_n = 2E_{ij}\overline{a}$, (39)

$\overline{S}_t = 8G_{ij}\overline{a}$, (40)

$G_{ij} = \left(\frac{2-\nu_i}{G_i} + \frac{2-\nu_j}{G_j}\right)^{-1}$. (41)

Table 9
Description of the parameters for the Johnson–Kendall–Roberts (JKR) contact model.

Parameter	E_{ij}	G_{ij}	r_{ij}	γ
Description	Equivalent Young's modulus	Equivalent shear modulus	Contact effective radius	Surface energy
Parameter	β_n	β_t	$\overline{u}_n^{rel}$	$\overline{u}_t^{rel}$
Description	Normal critical damping ratio	Shear critical damping ratio	Relative normal translational velocity	Relative tangential translational velocity
Parameter	$\overline{\theta}^{rel}$	m_{ij}	$\overline{\delta}_n$	$\overline{a}$
Description	Relative rotation angle	Equivalent mass of the particle	Normal overlap at the contact	Contact patch radius
Parameter	$\overline{\delta}_t$	μ_s	μ_r	k_t
Description	Tangential overlap at the contact	Coefficient of static friction	Rolling friction coefficient	Tangential stiffness coefficient

Table 10
Simulation parameters for DEM models.

Young's modulus (MPa)	**Density (kg/m^3)**	**Stiffness ratio**	**Poisson's ratio**	**Coefficient of restitution**
55,000	2650	2.6	0.3	0.2
Local damping	**Coefficient of static friction**	**Rolling friction coefficient**	**Surface energy (J/m^2)**	**Time step (s)**
0	0.5	0.35	0.155	8.0×10^{-8}

References

[1] Tian A, Li W, Yang M, Ding J, Pei L, Weng Y. A coarse aggregate particle size classification method by fusing 3D multi-view and graph convolutional networks. Comput-Aided Civ Infrastruct Eng 2025;40(7):940–58. https://doi.org/10.1111/mice.13369.

[2] Feng D. A compactor-soil coupling model considering mechanical inertia and its delayed feedback active suspension control. Int J Non Linear Mech 2025;179:105245. https://doi.org/10.1016/j.ijnonlinmec.2025.105245.

[3] Pouranian MR, Shishehbor M, Haddock JE. Impact of the coarse aggregate shape parameters on compaction characteristics of asphalt mixtures. Powder Technol 2020;363:369–86. https://doi.org/10.1016/j.powtec.2020.01.014.

[4] Yang L, Shi Z, Li K, Hu X, Shi C. Expansion of irregularly shaped aggregate induced by alkali-silica reaction: insights from numerical modeling. Cem Concr Res 2025;187:107727. https://doi.org/10.1016/j.cemconres.2024.107727.

[5] Yin T, Leng Y, Shu K, Liu K, Fan D, Wang S, et al. Effects of aggregate morphology and particle size distribution modulus on the rheological properties and microstructure of low water/binder cement-based composites (LW/B-CC). Powder Technol 2025;453:120608. https://doi.org/10.1016/j.powtec.2025.120608.

[6] Fan M, Su D, Wu D, Chen X. Reconstruction of irregular elongated/flattened particles and generation of particle aggregates with customizable form distributions. Powder Technol 2023;425:118553. https://doi.org/10.1016/j.powtec.2023.118553.

[7] Feng D, Fu C, Otto F, Hernandez AG, Liu P. Calibration of contact model parameters for aggregates: considering particle shape and moisture content. Powder Technol 2026;469:121771. https://doi.org/10.1016/j.powtec.2025.121771.

[8] Feng D, Fu C, Zheng K, Wang T, Wang C. Numerical framework for asphalt pre-compaction optimization using a coarse-graining discrete element method (DEM). Powder Technol 2026;478:122486. https://doi.org/10.1016/j.powtec.2026.122486.

[9] Liu H, Lu H, Zhu X, Yi Z, Yu X, Jin D, et al. Fatigue life of pre-cut seam asphalt mixture composite beams: a combined study of Fatigue damage evolution and reflective cracking extension. Buildings 2025;15(1):50. https://doi.org/10.3390/buildings15010050.

[10] Yu W, Wang S, Gong Z, Miao Y. Effect of compaction degree on the topological characteristics of force chain network (FCN) in aggregate blend. Constr Build Mater 2024;419:135554. https://doi.org/10.1016/j.conbuildmat.2024.135554.

[11] Wang S, Wang J, Wang J, Xu J, Miao Y, Ma Q, et al. Characterization of force distribution and force chain topology in asphalt mixtures using the discrete element method. Mater (Basel) 2025;18(10):2347. https://doi.org/10.3390/ma18102347.

[12] Wei X, Sun Y, Gong H, Li Y, Chen J. 3D identification and characterization of force chains in asphalt concrete based on continuum mesomechanics. Comput Struct 2024;297:107329. https://doi.org/10.1016/j.compstruc.2024.107329.

[13] Huang D-Q, Li P-D. Effect of aggregate sizes on dilation properties and stress–strain behavior of FRP-confined recycled aggregate concrete. J Build Eng 2024;89:109245. https://doi.org/10.1016/j.jobe.2024.109245.
[14] Li J-T, Gao C-B, Liu F-Y. Effect of particle size on shear behavior of Geogrid–Aggregate interface under cyclic normal loading. J Mater Civ Eng 2025;37(12):4025431. https://doi.org/10.1061/JMCEE7.MTENG-19031.
[15] Yu Y, Huang W, Sun M, Du X, Lin H. Effect of aggregate and void characteristics on shear resistance of asphalt mixtures. Processes 2025;13(11):3461. https://doi.org/10.3390/pr13113461.
[16] Peng X, Lv S, Huang T, Zheng C, Jiang M, Yuan J, et al. Performance check of asphalt mixture layer based on yield criterion and normalized fatigue equation. J Mater Civ Eng 2022;34(5). https://doi.org/10.1061/(ASCE)MT.1943-5533.0004205.
[17] Peng X, Yuan J, Wu Z, Lv S, Zhu X, Liu J. Investigation on strength characteristics of bio-asphalt mixtures based on the time–temperature equivalence principle. Constr Build Mater 2021;309:125132. https://doi.org/10.1016/j.conbuildmat.2021.125132.
[18] Mishra A, Carrara P, Griffa M, de Lorenzis L. Fracture in concrete: x-ray tomography with in-situ testing, digital volume correlation and phase-field modeling. Cem Concr Res 2026;199:108012. https://doi.org/10.1016/j.cemconres.2025.108012.
[19] Wei S, Zhang H, Wang D, Wang X, Cao M. Mesoscale mechanical analysis of concrete based on a 3D random aggregate model. Coatings 2025;15(8):883. https://doi.org/10.3390/coatings15080883.
[20] Hu X, Wan-Wendner L, Molkens T, Gruyaert E. A review on mesoscale modeling of recycled aggregate concrete—Advances, challenges, and perspectives. J Build Eng 2025;114:114272. https://doi.org/10.1016/j.jobe.2025.114272.
[21] Ding X, Liu F, Ma T, Xiao B. Effects of coarse aggregate morphology on asphalt mixture's flowability: parametric and prediction study. Case Studies in Construction Mater (Basel) 2024;21:e03735. https://doi.org/10.1016/j.cscm.2024.e03735.
[22] Peng X, Pan F, Lin Z, Lv S, Liu P. Experimental and molecular dynamics investigation of graphene oxide-modified bio-oil rejuvenated asphalt binder. Constr Build Mater 2025;494:143354. https://doi.org/10.1016/j.conbuildmat.2025.143354.
[23] Peng X, Xie N, Xia C, Zhou X, Zhao P, Ma S, et al. Laboratory evaluation of different bio-oil recycled aged asphalts: conventional performances and microscopic characteristics. J Clean Prod 2023;428:139442. https://doi.org/10.1016/j.jclepro.2023.139442.
[24] Wei S, Wang D, Wang X, Zhang H, Cao H, Liu Q. Research on the random generation model of 2D irregular aggregates in concrete based on fast grid region division method and its ground penetrating radar characteristics. Case Stud Constr Mater 2024;21:e03932. https://doi.org/10.1016/j.cscm.2024.e03932.
[25] Liu Q, Wei D, Gan Y. Mesoscale modelling of triaxial concrete fracture: the role of aggregate shapes. Int J Mech Sci 2025;302:110570. https://doi.org/10.1016/j.ijmecsci.2025.110570.
[26] El Haloui Y, Fakhari Tehrani F, Absi J, Courreges F, El Omari M, Allou F, et al. Modelling of asphalt mixes based on X-ray computed tomography and random heterogeneous generation. Int J Pavement Eng 2020;21(13):1626–37. https://doi.org/10.1080/10298436.2018.1559316.
[27] Ozturk HI, Rashidzade I. A photogrammetry based method for determination of 3D morphological indices of coarse aggregates. Constr Build Mater 2020;262:120794. https://doi.org/10.1016/j.conbuildmat.2020.120794.
[28] Tan Z, Jelagin D, Fadil H, Leng Z, Li R, Jiang J, et al. Virtual-specimen modeling of aggregate contact effects on asphalt concrete. Constr Build Mater 2023;400:132638. https://doi.org/10.1016/j.conbuildmat.2023.132638.
[29] Wan C, Zhong M, Yinghao Z. A study on the three-dimensional contact quantitative analysis of coarse aggregate in steel slag asphalt mixture based on X-ray CT. Case Stud Constr Mater 2024;21:e03600. https://doi.org/10.1016/j.cscm.2024.e03600.
[30] Spangenberg J, Roussel N, Hattel JH, Sarmiento EV, Zirgulis G, Geiker MR. Patterns of gravity induced aggregate migration during casting of fluid concretes. Cem Concr Res 2012;42(12):1571–8. https://doi.org/10.1016/j.cemconres.2012.08.007.
[31] Tan Z, Guo F, Leng Z, Yang Z, Cao P. A novel strategy for generating mesoscale asphalt concrete model with controllable aggregate morphology and packing structure. Comput Struct 2024;296:107315. https://doi.org/10.1016/j.compstruc.2024.107315.
[32] Yadav S, Das A, Singh S, Tomar S, Singh R, Singh M. Coupled approach and its convergence analysis for aggregation and breakage models: study of extended temporal behaviour. Powder Technol 2024;439:119714. https://doi.org/10.1016/j.powtec.2024.119714.
[33] Dai W, Yu H, Qian G, Ge J, Zhong Y, Zhang C, et al. Evaluation of compaction effect on void connectivity and aggregate distribution of porous asphalt (PA) mixture. Constr Build Mater 2025;482:141022. https://doi.org/10.1016/j.conbuildmat.2025.141022.
[34] Feng D, Guan J, Fu C, Hu Y, Otto F, Hernandez AG, et al. Augmentation of 3D virtual aggregate database using deep convolutional Wasserstein generative adversarial networks. Adv Eng Inform 2026;69:103994. https://doi.org/10.1016/j.aei.2025.103994.
[35] Zhang J, Nie R, Li Y, Tan Y. Random generation of three-dimensional realistic ballast particles using generative adversarial networks. Comput Geotech 2025;178:106923. https://doi.org/10.1016/j.compgeo.2024.106923.
[36] Feng D. Multi-scale algorithm for controllable virtual aggregate generation in mesoscale modeling. Int J Mech Sci 2025;308:110978. https://doi.org/10.1016/j.ijmecsci.2025.110978.
[37] Garcia-Hernandez A, Michot-Roberto S, Dopazo-Hilario S, Chiarelli A, Dawson A. Creation of realistic virtual aggregate avatars. Powder Technol 2021;378:760–71. https://doi.org/10.1016/j.powtec.2020.10.036.
[38] Jin L, Yu W, Li D, Du X. Numerical and theoretical investigation on the size effect of concrete compressive strength considering the maximum aggregate size. Int J Mech Sci 2021;192:106130. https://doi.org/10.1016/j.ijmecsci.2020.106130.
[39] Podlozhnyuk A, Pirker S, Kloss C. Efficient implementation of superquadric particles in discrete element method within an open-source framework. Comp Part Mech 2017;4(1):101–18. https://doi.org/10.1007/s40571-016-0131-6.
[40] Hoang UT, Nguyen NH. Particle shape effects on granular column collapse using superquadric DEM. Powder Technol 2023;424:118559. https://doi.org/10.1016/j.powtec.2023.118559.
[41] Hu X, Wan-Wendner L, Molkens T, Gruyaert E. Statistical generation of 3D mesoscale model for recycled aggregate concrete. Constr Build Mater 2025;476:141096. https://doi.org/10.1016/j.conbuildmat.2025.141096.
[42] Tong C-X, Li J-J, Sun Q, Zhang S, Zhou W-H, Sheng D. A noise-based framework for randomly generating soil particle with realistic geometry. Comput-Aided Civ Infrastruct Eng 2025;40(13):1829–46. https://doi.org/10.1111/mice.13424.
[43] Théodon L, Coufort-Saudejaud C, Debayle J. A stochastic model based on gaussian random fields to characterize the morphology of granular objects. Pattern Recognit 2024;149:110255. https://doi.org/10.1016/j.patcog.2024.110255.
[44] Kheradmandi N, Radenberg M. Employing 3D laser scanner for automated morphological assessment of aggregates produced from diverse sources and by different crushing methods. Constr Build Mater 2024;448:138034. https://doi.org/10.1016/j.conbuildmat.2024.138034.
[45] Yao B, Xu H, Wang Y, Guo P, Chen X, Xu H, et al. Optimization of aggregates skeleton using laser-scanning technology and discrete element method. Constr Build Mater 2023;408:133731. https://doi.org/10.1016/j.conbuildmat.2023.133731.
[46] Anochie-Boateng JK, Komba JJ, Mvelase GM. Three-dimensional laser scanning technique to quantify aggregate and ballast shape properties. Constr Build Mater 2013;43:389–98. https://doi.org/10.1016/j.conbuildmat.2013.02.062.
[47] Loz PHF, Angulo SC, Rebmann MS, Tutumluer E. Use of a 3D structured-light scanner to determine volume, surface area, and shape of aggregates. J Mater Civ Eng 2021;33(9):4021240. https://doi.org/10.1061/(ASCE)MT.1943-5533.0003824.
[48] Li R, Lu W, Chen M, Wang G, Xia W, Yan P. Quantitative analysis of shapes and specific surface area of blasted fragments using image analysis and three-dimensional laser scanning. Int J Rock Mech Min Sci 2021;141:104710. https://doi.org/10.1016/j.ijrmms.2021.104710.
[49] Fuchs L, Furat O, Finegan DP, Allen J, Usseglio-Viretta FLE, Ozdogru B, et al. Generating multi-scale Li-ion battery cathode particles with radial grain architectures using stereological generative adversarial networks. Commun Mater 2025;6(1):4. https://doi.org/10.1038/s43246-024-00728-5.
[50] Le VD, Go G-H. Application study on conditional generative adversarial network (cGAN) to generate ballast particles for discrete element method simulation. Case Studies in Construction Mater (Basel) 2025;23:e04987. https://doi.org/10.1016/j.cscm.2025.e04987.
[51] Michot-Roberto S, Garcia-Hernández A, Dopazo-Hilario S, Dawson A. The spherical primitive and perlin noise method to recreate realistic aggregate shapes. Granul Matter 2021;23(2):41. https://doi.org/10.1007/s10035-021-01105-6.
[52] Ma J, Ding W, Lin Y, Chen W, Huang L. A fast and efficient particle packing generation algorithm with controllable gradation for discontinuous deformation analysis. Geomech Geophys Geo-Energ Geo-Resour 2023;9(1):97. https://doi.org/10.1007/s40948-023-00637-w.
[53] Shen J, Wang B, Hou J, Yao P. Numerical study on the effect of coarse aggregate shape during concrete mixing process. Mater (Basel) 2024;17(7):1515. https://doi.org/10.3390/ma17071515.
[54] Zhang Z, Lu DX, Qiao Y, Giustozzi F. Modelling the hydraulic performance of open graded asphalt using the discrete element method and computational fluid dynamics. J Hydrol 2023;621:129612. https://doi.org/10.1016/j.jhydrol.2023.129612.
[55] Zhang W, Han L, Wang Z, Liu H, Wang L, Gao X. Generation of 3D geotechnical particles using random angular bend algorithm. Num Anal Meth Geomech 2023;47(8):1313–30. https://doi.org/10.1002/nag.3515.
[56] Ding Y, Lu Q, Lu F, Zhang X. A novel method for generation of particle packing model used in numerical simulation for the mechanical behavior of multi-component material. Mater Des 2022;216:110554. https://doi.org/10.1016/j.matdes.2022.110554.
[57] Jayasuriya A, Adams MP, Bandelt MJ. Generation and numerical analysis of random aggregate structures in recycled concrete aggregate systems. J Mater Civ Eng 2020;32(4):4020044. https://doi.org/10.1061/(ASCE)MT.1943-5533.0003113.
[58] Huang P, Zhao Y, Wu Y, Wang T, Zhao P. Rapid generation of 3D mesoscale concrete models using an improved GJK algorithm for collision detection. Buildings 2025;15(21):3883. https://doi.org/10.3390/buildings15213883.
[59] Guo C, Lu Z. A 3D FEM mesoscale numerical analysis of concrete tensile strength behaviour. Adv Mater Sci Eng 2021;2021(1):5538477. https://doi.org/10.1155/2021/5538477.
[60] Perlin K. Improving noise. ACM Trans Graph 2002;21(3):681–2. https://doi.org/10.1145/566654.566636.
[61] Worley S. A cellular texture basis function. In: International Conference on Computer Graphics and Interactive Techniques; 1996.
[62] Cheng H, Gupta KC. An historical note on finite rotations. J Appl Mech 1989;56(1):139–45. https://doi.org/10.1115/1.3176034.

[63] Wadell H. Volume, shape, and roundness of quartz particles. J Geol 1935;43(3):250–80.
[64] Wadell H. Volume, shape, and roundness of rock particles. J Geol 1932;40(5):443–51.
[65] Wadell H. Sphericity and roundness of rock particles. J Geol 1933;41(3):310–31.
[66] Attene M. Shapes In a box: disassembling 3D objects for efficient packing and fabrication. Comput Graph Forum 2015;34(8):64–76. https://doi.org/10.1111/cgf.12608.
[67] Russ JC, Neal FB. The image processing handbook. CRC Press; 2018.
[68] Zingg T. Beitrag zur Schotteranalyse. Zurich: ETH; 1935.
[69] Bhattacharyya A. On a measure of divergence between two multinomial populations. Sankhyā: Indian J Stat (1933-1960) 1946;7(4):401–6.
[70] Kullback S, Leibler RA. On information and sufficiency. Ann Math Stat 1951;22(1):79–86.
[71] Lin J. Divergence measures based on the Shannon entropy. IEEE Trans Inf Theory 1991;37:145–51.
[72] Xiao F, Amirkhanian SN, Putman BJ, Juang H. Feasibility of superpave gyratory compaction of rubberized asphalt concrete mixtures containing reclaimed asphalt pavement. Constr Build Mater 2012;27(1):432–8. https://doi.org/10.1016/j.conbuildmat.2011.07.024.
[73] Chen J, Huang B, Chen F, Shu X. Application of discrete element method to superpave gyratory compaction. Road Mater Pavement Des 2012;13(3):480–500. https://doi.org/10.1080/14680629.2012.694160.
[74] Dai W, Qian G, Zhu X, Yu H, Shi C, Zhang C, et al. Research on void characteristics during compaction of asphalt mixtures. Constr Build Mater 2024;416:135069. https://doi.org/10.1016/j.conbuildmat.2024.135069.
[75] Ge J, Yu H, Qian G, Dai W, Zhang C, Zhong Y, et al. Evaluation on the diffusion-fusion properties and interfacial mechanical behavior of virgin and aged asphalt. J Clean Prod 2024;477:143788. https://doi.org/10.1016/j.jclepro.2024.143788.
[76] Cundall PA, Strack ODL. A discrete numerical model for granular assemblies. Geotechnique 1979;29(1):47–65. https://doi.org/10.1680/geot.1979.29.1.47.
[77] Johnson KL, Kendall KA, Roberts D. Surface energy and the contact of elastic solids. Proc R Soc Lond A 1971;324:301–13. https://doi.org/10.1098/rspa.1971.0141.
[78] Deng R, Lu X, Ye T. The effect of JKR surface energy on the flowing property of fresh concrete in DEM simulation. Part Sci Technol 2024;42(5):789–803. https://doi.org/10.1080/02726351.2023.2291768.
[79] Moreno-Juez J, Tavares LM, Artoni R, de Carvalho RM, da Cunha ER, Cazacliu B. Simulation of the attrition of recycled concrete aggregates during concrete mixing. Mater (Basel) 2021;14(11):3007. https://doi.org/10.3390/ma14113007.
[80] Feng D, Fu C, Liu P. A modified Johnson-Kendall-Roberts contact model for pavement engineering: consideration of time-dependent surface energy. Powder Technol 2026;468:121701. https://doi.org/10.1016/j.powtec.2025.121701.
[81] Feng D. A DEM-based particle–force chain informatics framework for data-driven evaluation of pavement pre-compaction. Adv Eng Inform 2026;71:104402. https://doi.org/10.1016/j.aei.2026.104402.
[82] Feng D. Parameter sensitivity in DEM of aggregates for road and construction materials. Adv Powder Technol 2025;36(12):105116. https://doi.org/10.1016/j.apt.2025.105116.
[83] Gilbert EG, Johnson DW, Keerthi SS. A fast procedure for computing the distance between complex objects in three-dimensional space. IEEE J Robot Autom 1988;4(2):193–203. https://doi.org/10.1109/56.2083.
[84] Parteli EJR, Schmidt J, Blümel C, Wirth K-E, Peukert W, Pöschel T. Attractive particle interaction forces and packing density of fine glass powders. Sci Rep 2014;4:6227. https://doi.org/10.1038/srep06227.